Three-dimensional electroelastic modeling of the nucleation and propagation of the spin domains in spin-crossover materials

Nicolas di Scala [ORCID], Nour El Islam Belmouri [ORCID], Miguel Angel Paez Espejo, and Kamel Boukheddaden [ORCID][*]

Université Paris-Saclay, Université de Versailles-Saint-Quentin-en-Yvelines, Groupe d'études de la matière condensée,
Unité mixte de recherche No 8635, 45 Avenue des États Unis, 78035 Versailles, France

A three-dimensional version of the electroelastic model allowing the description of spin-crossover (SCO) materials taking into account for the volume change at the transition between the LS and the HS spin states is developed. The investigations are realized on a rectangular parallelepiped lattice with cubic symmetry. The SCO units are modeled by two-states fictitious spins coupled by springs whose equilibrium distances depend on the spin states. We implemented massive parallel simulations using CUDA (Compute Unified Device Architecture) programming where the spin states are updated using the Monte Carlo METROPOLIS algorithm, while the mechanical relaxation (lattice position) is performed by molecular dynamics. In this work, we investigated (i) the case of the thermal spin transition showing the macroscopic deformation of the parallelepiped accompanying the propagation of single domains and (ii) the isothermal relaxation of the photoinduced metastable HS fraction at low temperature. In both cases, the interplay between the electronic and the structural aspects of these transformations is analyzed and discussed in relation with the model parameters.

I. INTRODUCTION

Spin-crossover solids (SCO) [1–5] have an electronic configuration ranging between $3d^4$ and $3d^7$ (chromium, manganese, iron, and cobalt) with an octahedral symmetry and are surrounded by nitrogen atoms. They are fascinating prototypes of inorganic molecular complexes, extensively studied for their bistability at a molecular scale, which is an essential physical property for applications in the field of switchable molecular solids such as high density memory devices, numerical displays, or actuators [6–8]. In the case of Fe(II)-based SCO materials (which is the most studied in literature) with $3d^6$ configuration, the central transition-metal ion experiences a ligand field energy which lifts the degeneracy of the 5 d-orbitals of Fe(II) and splits them into three weakly bonding t_{2g} and two antibonding e_g orbitals. Depending on the strength of this ligand field, noted here Δ, and the intensity of the interaction between neighboring molecules, a competition between two spin states, namely, the diamagnetic low-spin (LS, $t_{2g}^6 e_g^0$, $S = 0$) state and the paramagnetic high-spin (HS, $t_{2g}^4 e_g^2$, $S = 2$) state does emerge. Thus the central metal ion is in the LS (HS) state when the value of Δ is much stronger (weaker) than the electrons pairing energy and the transition becomes thermally accessible when $\Delta \sim k_B T$, where T is the temperature. Locally, the spin transition from LS to HS is accompanied with the volume expansion of the molecular coordination sphere (around 30%) [9] which could be interpreted by the electrons redistribution between t_{2g} and e_g orbitals during the spin transition of the metal

ion, leading to the increase of the Fe-N bond lengths from $\sim$2.0 Å in the LS state to $\sim$2.2 Å in the HS state [3,10]. Although these local volume expansions are occurring at several points in the lattice, the global volume expansion of the whole network is only $\sim$3%–5% [11], this latter value is small compared to the volume expansion of the molecular coordination sphere. Indeed, a large part of the volume expansion is absorbed by the molecular structure of the lattice through ligand rotations and changes in the molecular packing. The spin transition can then be achieved when the pairing energy and the ligand field energy Δ are equivalent [12], and it can be controlled by many external parameters such as: temperature variation [13], external pressure [14–16], magnetic fields [17], or a light radiation (via the LIESST effect, standing for light induced excited spin state trapping; which is trapping at low temperature of HS metastable state by light) [18–20]. The LS-HS transition brings multiple changes in properties, such as magnetic, structural, optical, and vibrational changes at the transition. The state of the system can be characterized by the so-called HS fraction n_{HS}, which is the fraction of molecules in the HS state at a given set of parameters, mainly temperature, pressure. The behavior of n_{HS} brings information about the cooperativity of the system.

In the case of the thermally induced spin transitions, the literature reports a huge variety of spin transitions, depending on the intensity of the elastic interactions between molecules: a continuous gradual transition—corresponding to a Boltzmann population of two degenerate states—arises in weakly cooperative materials [21], while an abrupt transition or a first-order transition accompanied by hysteresis can be seen in strong cooperative systems [22].

*kamel.boukheddaden@uvsq.fr

The desire to understand cooperativity (its influence and its role in the transition) has led to the development of various theoretical models trying to explain the origin of the hysteresis phenomenon in SCO materials: mean-field approaches using phenomenological interaction parameters acting similarly for all molecules [3,23,24] or Ising-like approaches in which the interaction was written under a form of an exchange term [25–27]. These models, although simple, were able to catch essential aspects of the spin transition, reproducing the conditions of existence of the gradual and first-order SCO transitions. Nevertheless, these descriptions are qualitative and are not adapted to give details on the reasons of the true physical origin of the SCO phenomenon. A new class of elastic models was developped, where the interactions between the spin state of the molecule and the lattice were introduced, taking into account the lattice volume change at the transition: the mechanoelastic [28–30], anharmonic [31,32] or electroelastic models [33,34]. These "new models" were capable to explicate the experimental spatiotemporal behaviors of the SCO transition, observed by optical microscopy on single crystals [35,36]: the transition begins from a corner or edge of the crystal and expands over the entirety of the material with a well-defined HS/LS interface whose shape and orientation rely on the structural aspects of the crystal in the HS and LS phases. In these models, the molecules are modeled as ponctual sites interacting via springs with elastic constants depending on the spin states of the connected spins.

Numerical simulations have been performed on two-dimensional (2D) systems [28,33,37–41], but fewer for three-dimensional (3D) [42–49]. In this paper, we perform massive parallel simulations of an electroelastic model in 3D using conventional Monte Carlo algorithm for the evolution of electronic (spin) and a molecular dynamics algorithm for the structural (lattice parameter) degrees of freedom. For our numerical implementation, we use the Compute Unified Device Architecture (CUDA), released by Nvidia for their graphics accelerator boards, in order to improve the computation time of the simulations and increase the system size of the studied lattices.

In this paper, we investigate the thermal properties of the electroelastic 3D lattice, the macroscopic nucleation, growth, and propagation of the front transformation during the spin thermal transition in a 3D parallelipedic shaped system. Several interesting physical properties are studied throughout this work. Thus we first analyze the dependence of the width and the shape of the thermal hysteresis of the HS fraction on the strength of the nearest-neighbor (1*n*) elastic constant, and then perform a meticulous analysis on the dependence of this quantity along the three directions (1,0,0), (0,1,0), and (0,0,1) of the lattice. Next, we study the nucleation, growth and propagation mechanisms along the thermal transition as well as along the relaxation at low-temperature of the metastable HS state.

This manuscript is organized as follows: in Sec. II, we present the 3D electroelastic model used and the simulation method; Sec. III, present the results obtained from these simulations, and in Sec. IV, we conclude and outline some possible developments of this work.
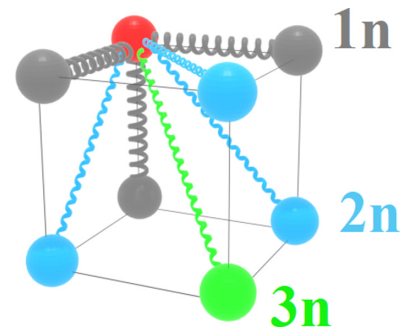
FIG. 1. Schematic view of the 3D elastic network within an elementary simulation cell for a test site represented in red, connected to its neighbors by springs represented in grey for the nearest neighbors (1*n*), in blue for the next-nearest neighbors (2*n*), and in green for the next-next-nearest neighbors (3*n*). The 1*n* neighbors are located along the edges of the cube, the 2*n* neighbors are located along the diagonals of the faces and the 3*n* neighbors are located along the long diagonals of the elementary cell.

II. NUMERICAL MODEL

A. 3D electroelastic model

As explained briefly in the introduction, we consider the electroelastic model in its 3D version which couples the electronic and the elastic properties of a SCO lattice. The model is based on the description of the HS and LS states of the *i*th SCO molecule of the lattice by a two-states fictitious spin S_i, with respective values $S_i = +1$ and $S_i = -1$ for HS and LS states, respectively. Each molecule is linked to its neighbors by an elastic spring, as depicted in Fig. 1, whose equilibrium distance depends on the spins of the neighbors. Thus we obtain an elastic network in which the nodes are made of spins and the intermolecular distances depend on these spin states by considering cubic unit cells in HS and LS phases. The equilibrium distance between two neighboring HS sites is naturally taken greater than that between two LS sites.

The total effective Hamiltonian of the system is given by

$$H = \sum_i (\Delta - k_B T \ln g)S_i + H_{\text{elast}}. \tag{1}$$

The first term in (1) corresponds to the electronic contribution, where Δ the ligand field energy gap, $g = g_{\text{HS}}/g_{\text{LS}}$ is the degeneracy ratio between the HS and LS states, T is the temperature, and k_B is the Boltzmann constant. The term $-k_B T \ln g$ is an entropic contribution originating from the difference of electronic and vibrational properties of HS and LS states. The temperature-dependence appearing in (1) lies in the fact that our system of two-state particles is characterized by eigenvalues $S = \pm 1$ with different associated degeneracies $g_\pm$. It is quite easy to demonstrate that an Ising-like Hamiltonian with and exchange interaction J and a field h with spins $S = +1$ and -1 having different degeneracies g_+ and g_-, is isomorphic with the usual Ising Hamiltonian with nondegenerate states having the same exchange interaction and a temperature-dependent field $h - kT \ln(g_+/g_-)$. A simple demonstration of this point by calculating the Boltzmann probability associated with a general configuration of spin states is given in [26] [Eqs. (A1) to (A3) of the Appendix].

TABLE I. Values of the nearest-neighbor equilibrium lattice parameters and elastic constants used in the simulations.

	Distances (nm)			Elastic constants (K nm^{-2})
1n distances	$R_0^{HH} = 1.20$	$R_0^{HL} = 1.10$	$R_0^{LL} = 1.00$	$A_{1n} = 3 \times 10^3$
diagonal faces	$\sqrt{2}R_0^{HH} \approx 1.70$	$\sqrt{2}R_0^{HL} \approx 1.56$	$\sqrt{2}R_0^{LL} \approx 1.41$	$B_{2n} = 0.3A_{1n}$
diagonal of the cube	$\sqrt{3}R_0^{HH} \approx 2.08$	$\sqrt{3}R_0^{HL} \approx 1.91$	$\sqrt{3}R_0^{LL} \approx 1.73$	$C_{3n} = 0.3A_{1n}$

The second term H_{elast} in (1) corresponds to the elastic contribution of the lattice, which is written here as

$$H_{\mathrm{elast}} = V_{1n}(|\vec{r}|) + V_{2n}(|\vec{r}|) + V_{3n}(|\vec{r}|)$$

$$= A_{1n}\sum_{(i,j)}(r_{ij} - R_0(S_i, S_j))^2 + B_{2n}\sum_{(i,k)}(r_{ik} - R_0'(S_i, S_k))^2$$

$$+ C_{3n}\sum_{(i,p)}(r_{ip} - R_0''(S_i, S_p))^2 \qquad (2)$$

Where 1n, 2n, and 3n denote the first-, second-, and third-nearest neighbors. Therefore, the elastic constants connecting a specific site (represented with a red sphere in Fig. 1) to its neighbors are given by: A_{1n} for nearest neighbors (1n) located along the three axes of the elementary simulation cell of the lattice (represented with grey spheres in Fig. 1), B_{2n} for next-nearest neighbors (2n) located along the diagonals of the faces of the cell (represented with blue spheres in Fig. 1), and C_{3n} for next-next-nearest neighbors (3n) located along the diagonals of the cell (represented with green spheres in Fig. 1).

The Euclidean distances are denoted to r_{ij} (respectively r_{ik} and r_{ip}) between the 1n sites i and j (respectively between 2n sites i and k, and 3n sites i and p). The equilibrium bond lengths between two 1n sites is $R_0(S_i, S_j)$ [respectively $R_0'(S_i, S_k)$ and $R_0''(S_i, S_p)$]. We denote by R_0^{HH}, R_0^{LL}, R_0^{HL} (R_0^{LH}), the equilibrium distances between 1n HS-HS, LS-LS, and HS-LS configurations. Thus we have $R_0(+1, +1) = R_0^{HH}$, $R_0(-1, -1) = R_0^{LL}$, and $R_0(+1, -1) = R_0(-1, +1) = R_0^{HL}$. Table I summarizes the values of the equilibrium lattice parameters, and elastic constants used in the simulations. For simplicity in this study, we assume that $R_0^{HL} = \frac{(R_0^{HH} + R_0^{LL})}{2}$, and we choose $B_{2n} = C_{3n}$ for the second and third neighbors.

The second- and third-nearest neighbors have been considered specifically to avoid shearing inside the lattice, and to ensure its stability. Moreover, the choice of $B_{2n} = C_{3n} = 0.3A_{1n}$ has been done to be consistent with previous works at 2D with elastic model [50], and thus enabling an easier comparison between results from different analysed systems, but with the same electroelastic model. In fact, even a very small value of 2n and 3n interactions are enough to realize the lattice stability even with open boundary conditions. However, increasing these elastic constants more than the values of the 1n elastic constants leads to other types of behaviors in the nucleation of the HS fraction. This part is interesting and deserves to be studied for its own as a separate work.

The simulations, and the results presented in this paper, have been performed using, as far as possible, realistic parameter values [51]: $\Delta = 450$ K and $g = 150$ leading to the equilibrium transition temperature of the Ising-like model $T_{\mathrm{eq}} = \frac{\Delta}{k_B \ln g} \approx 90$ K. According to the used values of

elastic constants, the bulk modulus, E, is roughly evaluated as A_{1n}/R_0, leading to a value of 5 GPa, which is in fair agreement with those reported in literature [52].

B. Simulation method

We consider a 3D parallelepipedic lattice of size $(N_x \times N_y \times N_z) = (96 \times 32 \times 32)$ with 98 304 spins, and free boundary conditions in order to consider for the macroscopic lattice deformation arising from local volume expansions/contractions resulting from the spin flips. The resolution of this model is based on an adaptation of code written in CUDA, developed for a similar 2D electroelastic model by our team [53]. This implementation takes advantage of the performance of Nvidia computing cores integrated in graphics accelerator boards: thanks to them, we can significantly improve the size of our simulation cells, without too much compromise with the computation time. When the code is executed, CUDA generates a grid of threads that are organized in a three-dimensional hierarchy. Each grid is organized into an array of thread blocks, where each one can contain up to 1024 threads and thread block size should be a multiple of 32 due to the multiprocessor of the cards wich can create, manage, schedule, and execute threads in groups of 32 parallel threads called warps. For each chosen simulation size of the system, the thread block size has to be well defined for a better efficiency. Thus very small block sizes, e.g., 32 threads per block, may limit performance due to occupancy, whereas very large block sizes for example 1024 threads per block, may also limit performance. The graphics accelerator boards used is a Nvidia RTX A5000 based on the Ampere architecture with 8192 cores, 24 GB GDDR6 memory available, a single precision performance up to 27.8 TFLOPS, and the CUDA driver version installed is 11.4.

We implement two different approches to solve Hamiltonian (1): one for the evolution of electronic (spins) degrees of freedom, and another one for the structural aspects by performing respectively a Monte Carlo METROPOLIS simulation (MC) on spin states combined with a simulation of molecular dynamics (MD) to relax mechanically the lattice positions.

1. Monte Carlo Metropolis algorithm and simulations methodology

First of all, we initialize the elastic network by setting up the initial positions of the sites and their initial desired spin values (for example all spins $S = +1$ and all distances $r_{ij} = R_0^{HH}$), and then we let the lattice relax mechanically to reach its equilibrium if necessary.

Afterwards, we use a parallelized MC algorithm over the spin states ($S = -1$ and $+1$) to realize their thermal switching. Thus there is no true magnetic (exchange) interactions

in the model where the spins interact through the elastic lattice (i.e., the springs). Thus each spin site represents a spin-crossover molecule whose degrees of freedom are defined by its spin value ± 1 and its coordinates (x, y, z) in the lattice. The entire spin network is divided into sublattices which are then mapped onto thread blocks, where each of the sublattice/block contains $(16 \times 4 \times 4) = 265$ threads, representing 256 molecules, that are also called sites or nodes through the paper. Overall, this forms a three-dimensional grid of $(6 \times 8 \times 8) = 384$ thread blocks. These blocks are contiguous, as the sites inside each block: we subdivide the spin lattice into multiple blocks in order to improve the computational time. We update the entire spin lattice in a parallel way at a frozen lattice configuration. In other words, we do not update the spins until we finish testing all the sites, this implies that whatever is the order in which we test the site and whether the blocks are contiguous or not, it does not change the result. Our GPU can perform operations on up to 8192 threads simultaneously. Indeed, the GPU is built on an array of Streaming Multiprocessors (64 in our case), where each Streaming Multiprocessors has a total of 128 cores and performs operations on only one thread block at a time. In addition, the order in which thread blocks are scheduled on the Streaming Multiprocessors, is decided by the hardware at runtime. Indeed, in CUDA each block of threads is scheduled (independently from the others) on any of the available multiprocessors within the GPU, in any order, concurrently or sequentially, so that the program can be executed on the maximum number of multiprocessors. The spin flip procedure is done by the usual Monte Carlo technique based on METROPOLIS transition probabilities. This METROPOLIS procedure is performed with random numbers obtained by a pseudorandom numbers' algorithm of high statistical quality, thanks to the library cuRand integrated in CUDA. To summarize, we select 8 192 sites i among the $N_x \times N_y \times N_z$ sites of the lattice, with spin values $\{S_i\} = \pm \{1\}_i$ and position vectors $\{\vec{r_i}\}$, and new spin value $\{S_{i\ \text{new}}\} = -\{S_i\}$ are set without changing the lattice positions. Each spin change is accepted or rejected by the usual MC METROPOLIS criterion. We store $\{S_{i\ \text{new}}\}$ in a different vector and we repeat the procedure for the next 8192 sites until all the 98 304 sites of the entire spin lattice are inspected for the spin change. Next, we relax mechanically the whole lattice through a molecular dynamics algorithm described below. Thus, in the procedure all lattice positions are updated 300 times at fixed spin configuration. We define this as the unit time of Monte Carlo procedure (MCS). We would like to highlight that this numerical procedure is not a cluster algorithm, like the Swendsen-Wang one [54]. It is interesting to mention that we could test 8192 noncontiguous spins, update them and relax the system mechanically, then test the next 8192 spins and so on. However, this method significantly slows down the simulation due to conflicts in accessing memory. This is why we test all spins before updating and relaxing.

2. Molecular dynamics algorithm

After all spins update, the elastic lattice is relaxed in a deterministic way to reach the stable mechanical state in a parallel way: each computing core calculates the gradient of potential energy of each site of equation (1), in order to determine the force vector, $\vec{F} = -\vec{\nabla} H_{\text{elast}}$, acting on every molecule or site. The obtained force field over the whole system is then normalized with the larger norm of the gradient, and the lowest energy configuration is searched by relaxing the system in overdamped dynamics with a time step $dt^2 = 0.001$ (and setting the value of the discretization step for the finite differences at 10^{-5}). This is the principle of the well-known steepest descent algorithm, useful to find the local minimum of the elastic energy landscape. The new positions of the molecules are recalculated using this new force field with a strong damping to avoid oscillations. This procedure is repeated 300 times, the aim being to reach the equilibrium state, which can be monitored with the time dependence of the total elastic energy of the system, which reaches a minimum averaged value.

We consider that every molecule has a damped oscillatory-type motion. The system of coupled differential equations for all molecules is $m \frac{d^2 \vec{r_i}}{dt^2} = \vec{F_i} - \mu \frac{d \vec{r_i}}{dt}$, where $\vec{r_i}$ is the Cartesian site position vector of site i and m is the mass of the particle, μ is the damping factor. In the case of overdamped dynamics, this equation becomes $\frac{d \vec{r_i}}{dt} = \frac{1}{\mu} \vec{F_i}$, where $\vec{F_i}$ is the total force acting on site i. If one considers only next-nearest elastic constants, the time scale of the dynamics is then $\sim \frac{\mu}{A_{1n}}$. The dynamics is stopped when the force on each node approaches zero. As a general observation, the MC time, given in Monte Carlo steps, is purely artificial and is hard to connect with any real dynamics or real experimental timescale. Molecular dynamics (MD) time is connected with the elastic constants and the damping constant, however, one can easily modify the time step ($dt^2 = 0.001$) or the number of MD iterations (here 300) performed between the selection of two successive spins for the MC process. A low number of MD iterations means that the lattice is not completely relaxed after each spin update, which makes the MD and MC processes competing. In the present MD simulations, we have chosen for practical reasons and also for the sake of simplicity, to well relax the lattice (300 MD iterations) after each MC spin update, and therefore the MD and MC dynamics are well separated. In other words, the lattice dynamics is assumed to be faster than the spin state relaxation. Indeed, usually the lattice relaxation is in the picosecond timescale, while the spin-state relaxation, that is the relaxation of the HS and LS states of the molecule, is in the range of the micro to nanoseconds as it has been observed in old Mossbauer experiments [55–57] in noncooperative spin-crossover materials where the fluctuations of the spin state of the molecule falls in the timescale of the Mossbauer technique (10^{-8} s) leading to widen the spectra when the frequency of the HS to LS fluctuation crosses that of the observation technique.

It is worth mentioning that using 0 K molecular dynamics simulation may lead the lattice subsystem to fall into a metastable state. However, since we allow spin state fluctuations in the MC process which affect the lattice energy, because of spin-distortion interaction, it is always possible to leave these metastable states in a reasonable finite time, except when the simulations are done at very low temperature, which exponentially increases the lifetime of the metastable states. Although, this type of dynamics is also used by other authors
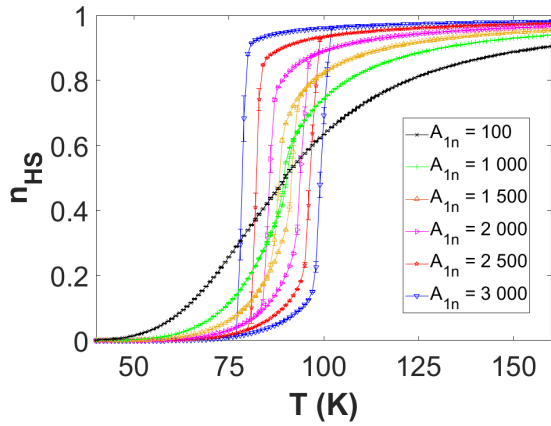
FIG. 2. Thermal dependence of the HS fraction n_{HS} for different values of elastic constants A_{1n} with error bars representing the standard deviation on the average n_{HS} for each temperature for the simulation cell size ($96 \times 32 \times 32$). Remark: each presented point has an error bar; however, the latter are visible only near the HS-LS transition, above and below the size of the error bars is smaller than the size of the points.

FIG. 3. Hysteresis width ΔT as a function of the square of the elastic constant values A_{1n} above the critical threshold A_{1n}^C showing a linear behavior. We take the values of $A_{1n} \geqslant 100$ K nm^{-2}, which are more easily measurable. In blue, we plot a linear regression with 95% confidence bounds.

when treating 2D and 3D mechanoelastic systems [29]. Nevertheless, performing finite temperature Verlet or Nose-Hoover algorithms would allow to have the same temperature for the spin and lattice subsystems, but it would lengthen the computational time simulations.

3. Measurements and calculations

The numerical simulations on temperature are done, thanks to the previous two algorithms, by using a defined amount of MCS as a waiting time to reach the stationary states at each temperature: the number of MCS depends of the simulation parameters and is defined empirically (typically $N_{therm}^{MCS} = [100, 500]$, depending of the elastic constant value A_{1n}). The temperature sweep rate is taken to 1 K every N_{therm}^{MCS} steps. Then, over the next 50 MCS, statistics are made to determine average physical values, like the HS fraction $n_{HS}(T)$, the mean distance between molecules, etc. Each averaged measurement is carried out after performing three independent runs to ensure that the different configurations used for means are statistically independent, so as to obtain uncorrelated equilibrium states.

For example with an elastic constant value $A_{1n} = 3000$, for each temperature step the simulation takes about 5 min 30 sec for a number $N_{therm}^{MCS} = 500$ with CUDA: the time needed to perform a thermal cycling of Fig. 2 is about 22 hours for the $A_{1n} = 3000$ case. For comparison, in sequential (on a desktop computer with Intel Core i5-10500 at 3.10 GHz with 27.953 MFLOPS and 32 GB of memory), for the same parameters, it would take about 1 hour and 35 min for each temperature step, and then about 16 days for the same thermal cycle in the $A_{1n} = 3000$ case. Thanks to our parallel computing with CUDA, here we enhance the calculation time by a factor 17.

The HDF5 library [58] is used for writing into files the spin state, the position and other configuration's information in order to store, manage and do postprocessing on them easily.
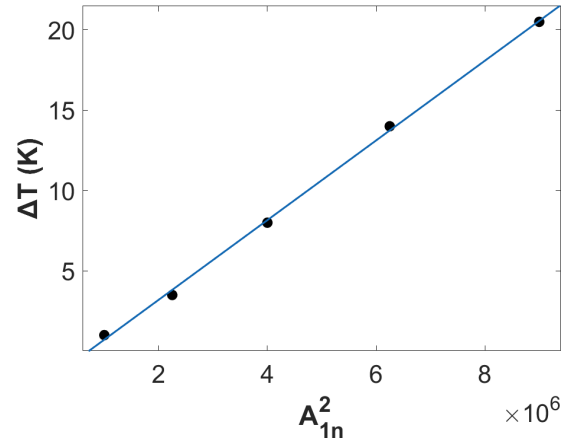
III. RESULTS

A. Thermal spin transition

The thermal properties of the electroelastic 3D lattice is monitored by the HS fraction $n_{HS} = \frac{(1+\langle S_i \rangle)}{2}$ as a function of T. Figure 2 represents the thermal hysteresis loop of our 98 304 spins for various elastic constant values A_{1n}. We observe that in the absence of any kind of interactions ($A_{1n} = 0 = B_{2n} = C_{3n}$), the thermal transition is smooth and gradual, and no hysteresis is detected. For low elastic constant values A_{1n}, the hysteresis is also undetectable. When the magnitude of elastic interactions is larger than a critical value, $A_{1n}^C = 250$, a hysteresis does appear: its shape and width depend on these interactions, becoming larger and more abrupt for more important values of A_{1n}. This expected behavior is similar to the experimental situations where compounds with strong interactions between the SCO complexes show wider hysteresis. We also notice that larger values of A_{1n} involve a squarer thermal hysteresis loop as observed in other 2D and 3D studies [43,59].

The width of the hysteresis ΔT is defined as a temperature interval between the heating T_{up} and the cooling T_{down} branches. These temperatures are defined as equilibrium temperatures at $n_{HS} = \frac{1}{2}$, and so $\Delta T = T_{up} - T_{down}$. As can be seen in Fig. 3 where we plot the hysteresis width ΔT as a function of elastic constant values A_{1n} above the critical threshold A_{1n}^C, we realize that the dependence of ΔT follows a power law almost parabolic. We plot a nonlinear regression with a power law $\Delta T = f(A_{1n}^2)$ where a 95% confidence is found. Of course, this dependence does not take into account others physical parameters of the system (different sizes of the simulation cell, elastic constants of the B_{2n} and C_{3n} neighbors, lattice misfit between HS and LS, etc.) whose slope may depend, which should be considered in a more detailed study to verify whether this power law exponent $\beta \approx 2$ can fall in a universality class at 3D or not.

Since we have a 3D lattice, we want to study the effect of the shape anisotropy of the system by analyzing the n_{HS}

(a) 96 planes of spins perpendicular to the (Ox) direction.

(b) 32 planes of spins perpendicular to the (Oy) direction.

(c) 32 planes of spins perpendicular to the (Oz) direction.
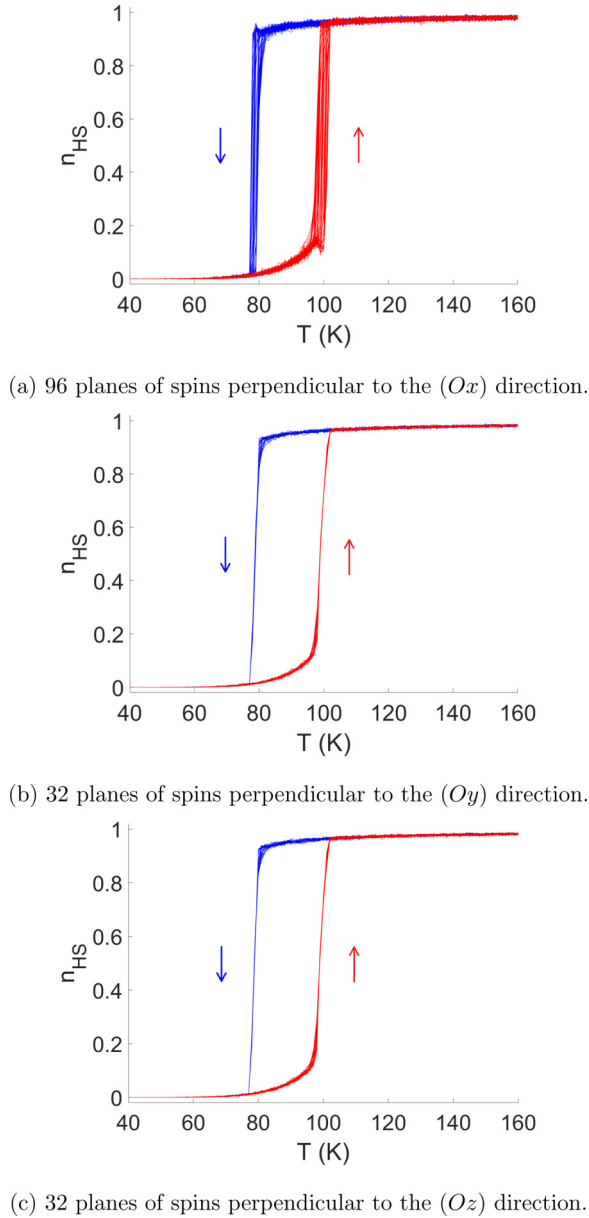
FIG. 4. Mean n_{HS} fraction as a function of T for each of the N_i planes of spins, perpendicular to the (Oi) direction, with $i = \{x, y, z\}$. Remark the cascade effect along (Ox) direction and the simultaneous transitions of all planes along (Oy) and (Oz) directions.

fraction for each plane of spins along the three directions of space. For instance in the (Ox) direction, we have sliced the simulation cell in perpendicular planes (yOz) at each spin node along the (Ox) direction, and we calculated the mean n_{HS} fraction in each of the 96 planes. Figure 4 shows the hysteresis loop as a function of T for each of the N_i planes of spins, perpendicular to the (Oi) direction, with $i = \{x, y, z\}$. We observe that there is a privileged direction for the propagation of the spin transition inside the system along the (Ox) direction, that is the elongated direction of the simulation cell. As a matter of fact, in that direction, we can see a cascade effect of the perpendicular spin planes that flip during the heating or the cooling branches of the loop at the approach of the transition temperature $T_{eq} \approx 90$ K, whereas there is
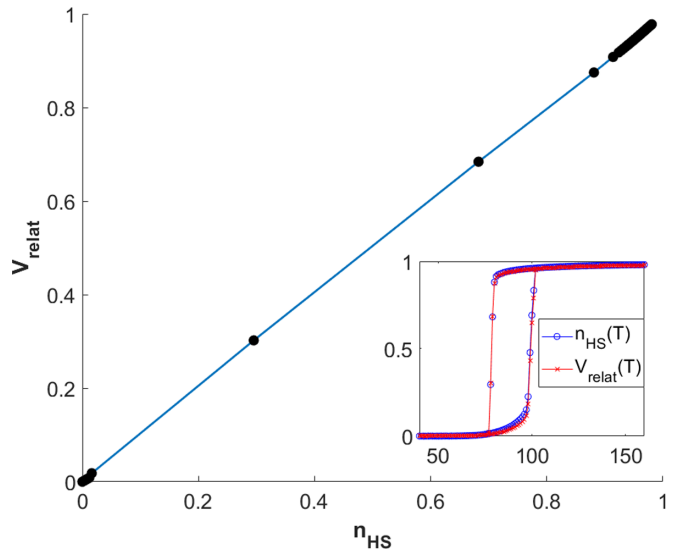
FIG. 5. Elastic variations of the lattice V_{relat} as a function of electronic variations n_{HS} during hysteresis loop presented for the case of the cooling branch for $A_{1n} = 3000$ for illustration. The same results are found for the heating branch, or for others elastic constant values. (Insert) The two considered variations V_{relat} and n_{HS} as a function of T.

no cascade effect in the (Oy) and (Oz) directions where the spin transition takes place simultaneously in all perpendicular planes. The difference between the transition temperature, between the transformation along (Ox) and both (Oy) and (Oz) directions is mainly attributed to bulk transformation for (Ox) and transitions on lattice surfaces for (Oy) and (Oz).

We are also interested in elastic variations of the lattice. For that, we compute the volume of the simulation cell as a function of T, and then we calculate the relative volume change, $V_{relat} = \frac{V(T) - V_{LS}}{V_{HS} - V_{LS}}$, where V_{LS} and V_{LS} are respectively the volume of the simulation cell when all spins are in the LS or HS state. To compare the changes of electronic n_{HS} and elastic V_{relat} order parameters, in the Fig. 5, we represent $V_{relat}(T)$ vs $n_{HS}(T)$ for the case of the cooling branch for $A_{1n} = 3000$. The two variations align perfectly, meaning that there is a good correlation between the behavior of the electronic and the mechanical properties during the thermal transition. We show in insert the two variations as a function of T for information. The same results are found for the heating branch, or for others elastic constant values, when hysteresis appears in the system. As a note, this result relates to the lifetime of the metastable states around the thermal hysteresis and the interplay between the dynamics of the spin and lattice degrees of freedom. Indeed, according to the simulation procedure in which the system is sufficiently relaxed mechanically (300 runs), after each spin flip, the volume follows adiabatically the behavior of the HS fraction, as shown in Fig. 5, where V_{relat} and n_{HS} are superimposed. Conversely however, if we perform the simulations with less molecular dynamics runs (for example, 10 instead of the previous 300, to exaggerate the effect) after each spin flip, then the lattice relaxation will interfere with that of the spin network and the thermal responses of V_{relat} and n_{HS} will be different with wider thermal hysteresis, see the Fig. S1 of Ref. [60].
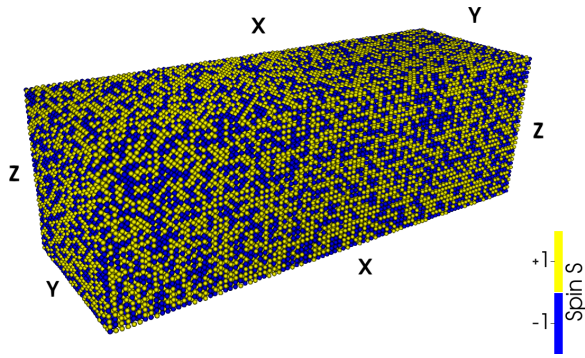
FIG. 6. Snapshot showing the spatiotemporal configurations of the lattice during the cooling branch at $n_{\mathrm{HS}} = 0.55$ and $T = 92$ K for $A_{1n} = 50$. Yellow (blue) spheres represent HS (LS) sites.

Furthermore, as illustrated in Fig. S2 of Ref. [60], we notice that the thermal evolution of the averaged $1n$, $2n$, and $3n$ distances of the neighboring pairs throughout the lattice follows the same trend as the thermal dependence of the HS fraction n_{HS}. Moreover, we note that the extrema values of these averaged distances are consistent with the nearest-neighbor equilibrium lattice parameters defined in Table I.

B. Spatiotemporal aspects of the nucleation, growth, and propagation of the spin states

The thermal dependence of the order parameters, n_{HS} and $\langle r \rangle$, allow to distinguish gradual transition from first-order, but don't bring any information about the spatial mechanism on the organization of the spin states along the transition. Here, we aim to investigate these aspects for the case of the thermally induced SCO transition, as well as the special case of low-temperature relaxation of metastable HS states.

1. Along the thermal transition

Figure 6 displays the spatial organization of the spin states for $n_{\mathrm{HS}} = 0.55$, for a value of A_{1n} below the critical value (here $A_{1n} = 50$), showing a random switch of the spin inside the simulation cell, in agreement with the weak cooperative character of the elastic interactions, compared to ligand field energy. Whereas value $A_{1n} = 3000$ above the critical value lead to the formation of clusters in the lattice configuration as depicted in Fig. 7. In the latter, the propagation of the spin transition inside the system corresponds to multiple domains of flipped spins that start independently from all corners and grow toward the center of the lattice.

We are interested in the lattice strain during the thermal procedure focusing on the study of the displacement field of lattice spins of the spatial configurations Figs. 6 and 7. As we have done previously for 2D systems [33,51], we denote by $\overrightarrow{u}(i, j, k)$ the displacement field associated with the spin coordinates (i, j, k), whose expression is defined by the following equation: $\overrightarrow{u}(\overrightarrow{r}) = \overrightarrow{u}(i, j, k) = \overrightarrow{r}(i, j, k) - \overrightarrow{r_0}(i, j, k)$, where $\overrightarrow{r}(i, j, k)$ and $\overrightarrow{r_0}(i, j, k)$ are respectively the final and initial positions of the spin vectors (i, j, k) in the lattice. We take the positions of the LS state as reference initial positions: $\overrightarrow{r_0}(i, j, k) = (i\ R_0^{LL}, j\ R_0^{LL}, k\ R_0^{LL})$. Elements of the strain tensor $\varepsilon_{\alpha\beta}$ ($\{\alpha, \beta\} = \{x, y, z\}$), given by:
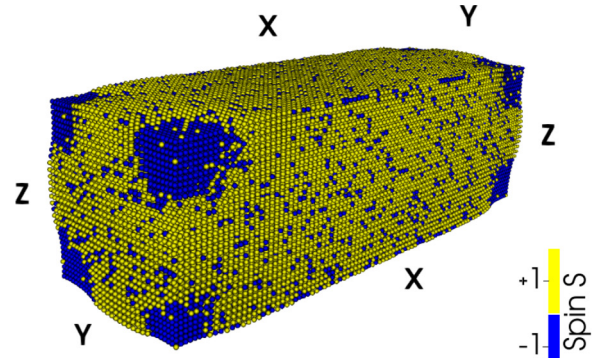
(a) $n_{HS} = 0.87$ at $T = 79K$
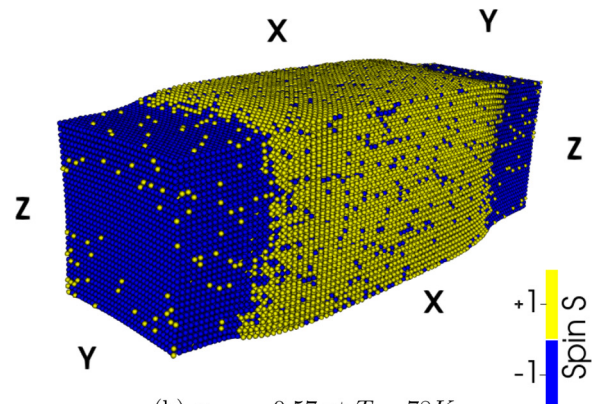
(b) $n_{HS} = 0.57$ at $T = 78K$
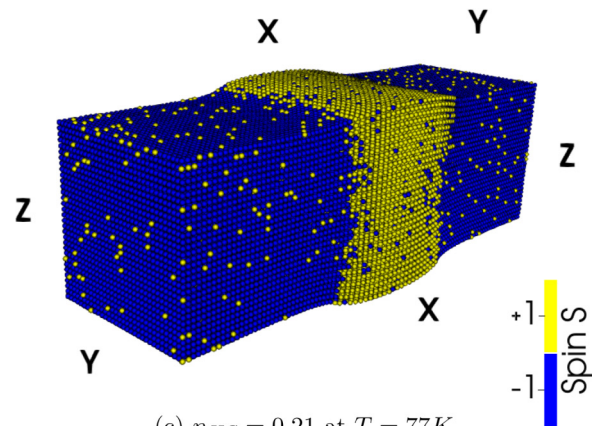
(c) $n_{HS} = 0.21$ at $T = 77K$

FIG. 7. Selected snapshots showing the spatiotemporal configurations of the lattice during the cooling branch at various n_{HS} values: 0.87 (a), 0.57 (b), and 0.21 (c) for $A_{1n} = 3000$. Yellow (blue) spheres represent HS (LS) sites. Remark the macroscopic domain character of the HS $\rightarrow$ LS transformation.

$\varepsilon_{\alpha\beta} = \frac{1}{2}(\frac{\partial u_\alpha}{\partial \beta} + \frac{\partial u_\beta}{\partial \alpha})$, bring information about the mechanical effects induced by the growth areas. Here, the derivatives of the various components of the displacement field are calculated within the approximation of continuous medium, for example, $\frac{\partial u_x}{\partial x} = \frac{u_x(i+1,j,k)-u_x(i,j,k)}{R_0^{LL}}$, $\frac{\partial u_y}{\partial y} = \frac{u_y(i,j+1,k)-u_y(i,j,k)}{R_0^{LL}}$, $\frac{\partial u_z}{\partial z} = \frac{u_z(i,j,k+1)-u_z(i,j,k)}{R_0^{LL}}$. Others derivatives $\frac{\partial u_x}{\partial y}$, $\frac{\partial u_z}{\partial y}$, etc. bringing information about deviatoric strain are calculated in the same way. In particular, the divergence of the displacement

(a) $n_{HS} = 0.87$ at $T = 79K$

(b) $n_{HS} = 0.57$ at $T = 78K$

(c) $n_{HS} = 0.21$ at $T = 77K$
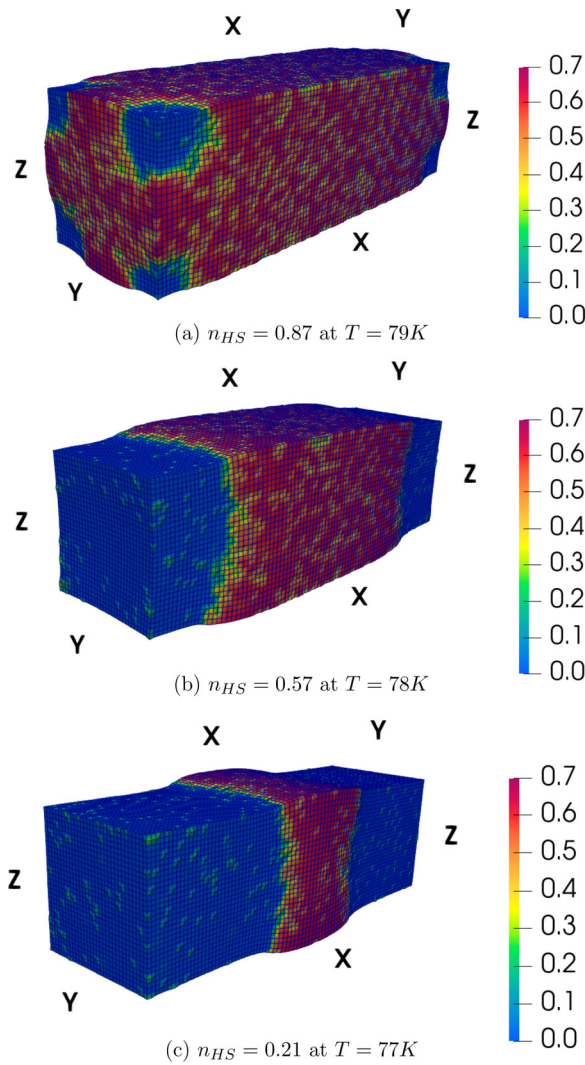
FIG. 8. Snapshots showing the spatial distribution of the divergence of the displacement field along the cooling branch of the thermal SCO transition, corresponding to snapshots of Fig. 7.

field, the expression of which is $\overrightarrow{\nabla} \cdot \vec{u}(\vec{r}) = \varepsilon_{xx}(\vec{r}) + \varepsilon_{yy}(\vec{r}) + \varepsilon_{zz}(\vec{r})$, that is the trace of the strain tensor which describes the local relative volume expansion and gives information about mechanical effects inside the simulation cell, allows to highlight the elastic character of the LS-HS interface during the transition.

Figure S3 of Ref. [60] and Fig. 8 show the spatial distribution of the divergence of the displacement field during hysteresis loop corresponding to snapshots of spins configurations of Figs. 6 and 7. Since the reference state is that of LS, this leads to a map of the divergence going from zero (in the LS state—bluish in the figures) to positive values (in the HS state—reddish in the figures). We realize that for $A_{1n} = 50$, below the critical value of elastic constant, the strain is randomly distributed in the simulation cell, as depicted in Fig. S4 of Ref. [60] illustrating different sectional views, wheres for $A_{1n} = 3000$, above the critical value, the most important changes occur in the interface regions as can be seen thanks to the sectional views of Fig. 9. A correlation is of

course observed between the divergence of the displacement field (dilation of the system) and the spins configurations. Furthermore, the interface shape is almost straight and perpendicular to the simulation cell border. In contrast, Figs. 9(b) and 9(c) clearly indicate that, contrary to the corresponding electronic interface of Figs. 7(b) and 7(c), the divergence field diffuses far from both sides of the interface, demonstrating the long-range character of the transformations operating in the simulated material.

Information about the shear stresses, which causes the distortion of the lattice during the spin transition, are given by the curl of the displacement field $\overrightarrow{\nabla} \times \vec{u}(\vec{r})$. This curl can be written in term of the rotation vector $\overrightarrow{\omega}$ by the relation $\overrightarrow{\nabla} \times \vec{u}(\vec{r}) = 2\overrightarrow{\omega}$. Elements of the rotation tensor $\omega_{\alpha\beta}$ are given by the equation $\omega_{\alpha\beta} = \frac{1}{2}(\frac{\partial u_\alpha}{\partial \beta} - \frac{\partial u_\beta}{\partial \alpha})$. This tensor is skew symmetric: $\omega_{\alpha\beta} = -\omega_{\beta\alpha}$, it has only three independent scalar components defining the rotation vector $\overrightarrow{\omega}$, with ω_i ($i = \{x, y, z\}$) components signifying the i axis around which there is a rotation. The components are $\omega_x = \frac{1}{2}(\frac{\partial u_z}{\partial y} - \frac{\partial u_y}{\partial z})$, $\omega_y = \frac{1}{2}(\frac{\partial u_x}{\partial z} - \frac{\partial u_z}{\partial x})$ and $\omega_z = \frac{1}{2}(\frac{\partial u_y}{\partial x} - \frac{\partial u_x}{\partial y})$. We have calculated the averages of each of the three component ω_i during the thermal cycle, for $A_{1n} = 50$ (gradual transition) and for $A_{1n} = 3000$ (hysteretic transition) whose respective results are summarized in Figs. 10(a) and 10(b). We note that for gradual transition the same kind of thermal evolution for the three component appears, with weak oscillations around a mean value (equal to zero for ω_x), and almost a symmetric behavior for ω_y and ω_z relative to x coordinate. This implies that rotational effects arise specifically around the y and z axes in the system. In contrast, for $A_{1n} = 3000$, while similar general trend is observed for the three components, an hysteresis is perceptible, but only for ω_y and ω_z. This hysteresis occurs for both of them exactly at the same temperatures, that is between $T = 79$ and 99 K, which also correspond to the switching temperatures found in the corresponding thermal behavior of the HS fraction. For further investigations, we compare the spatial distribution of the curl of the displacement field with previous results at $A_{1n} = 3000$. As can be seen in Figs. S4–S8 of Ref. [60], we observe different behaviors in the curl of the displacement field between the heating and the cooling branches. A correlation between the curl of the displacement field, the spatial distribution of the divergence (and the electronic interface) is found for the heating branch, but during the cooling one, the changes in the curl starts some Kelvins before the interface propagation (more precisely in the same interval of temperatures where the distortion of the lattice occurs during the heating branch, i.e., around the equilibrium temperature of the heating branch which is $T_{up} \approx 99$ K at $n_{HS} = 1/2$ via Fig. 2), which can be then seen as a precursor phenomena announcing the occurrence of the front propagation event. More details about this peculiar behavior are given in Ref. [60].

2. Along the relaxation at low-temperature of the metastable HS state

We are now interested in the mechanism of relaxation of the metastable HS state at low-temperature. Such a metastable state can be obtained experimentally by

(a) $n_{HS} = 0.87$ at $T = 79K$ (b) $n_{HS} = 0.57$ at $T = 78K$

(c) $n_{HS} = 0.21$ at $T = 77K$
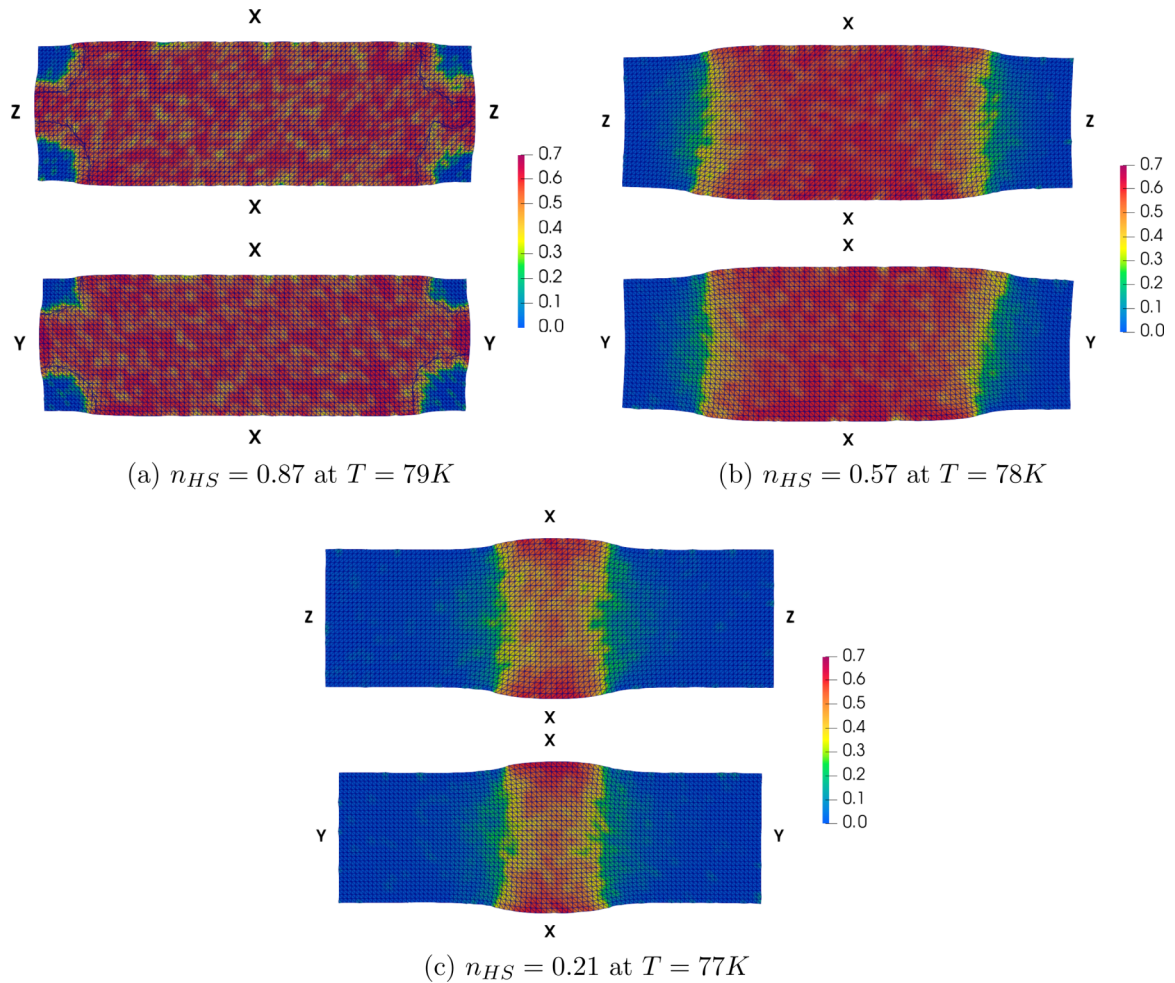
FIG. 9. Sectional view in the planes (xOz) and (xOy): (a) at N_y (top) and N_z (bottom), and at $\frac{N_y}{2}$ (top) and $\frac{N_z}{2}$ (bottom) for (b) and (c), of the spatial distribution of the divergence of the displacement field corresponding to snapshots of Fig. 8.

photoexcitation (LIESST effect) or by rapid quenching of the high-temperature stable HS state. Here, the lattice is initially prepared in the HS state from both electronic ($S_i = +1$, $\forall i$) and structural ($r_{ij} = R_0^{HH}$) point of view. This configuration is naturally metastable at low temperature and, consequently, the system is expected to relax towards the LS state. We perform such a relaxation isothermally at $T = 1$ K to minimize thermal fluctuations. Through that approach, we want to understand the effects of the elastic constant values A_{1n} on the nucleation and growth processes of the LS domains and their propagation through the present 3D lattice within the present Hamiltonian.

Numerically, we measure n_{HS} every MCS from 0 to 400 MCS. The shape of the relaxation curves of the HS fraction, n_{HS}, of Fig. 11(a), which changes from exponential or stretched exponential to sigmoidal, indicates, as expected, a shift from weak cooperative to strong cooperative behavior when increasing elastic constant values A_{1n}. We have outlined the same elastic values of A_{1n} as in Fig. 2, but we have added more values above the critical threshold $A_{1n} = 4000, 5000, 6000, 7000,$ and 8000. The calculations of the isothermal relaxation curves are less time-consuming than the thermal process, that is why we added them here to highlight the behavior at large A_{1n} values. We can see that the lifetime of the metastable HS state increases in the beginning of the

relaxation curve for large values of A_{1n}, supporting the fact that there is an increase in the elastic energy barrier to overcome for a spin to flip from an HS to LS state. It is interesting to comment about the sigmoidal shape of the HS fraction curves in the case of strong cooperative systems ($A_{1n} \geqslant 6000$). There, two regimes are obtained: the first one is characterized by a slight decrease of the HS fraction during the 100 MCS for $A_{1n} = 7000$, followed by a new regime where the HS fraction falls down almost linearly on time. By inspecting the time evolution of the average nearest-neighbor bond lengths ($\langle r_{1n} \rangle$), represented in Fig. 11(b), one sees that during the so-called first regime, which is in fact a stochastic regime, the lattice is already moving towards the LS structure, by nucleating small LS domains (here mainly in the corners). The second regime is then a kind of a flow regime, where the lattice has overpassed the elastic energy barrier preventing the relaxation. In this regime, the front interface travels at almost constant velocity, which results in the linear behavior of the HS with time. For $A_{1n} \lesssim 1000$, corresponding to weak elastic energy barriers, "exponential-shaped" relaxation curves, suggest that only the second deterministic regime is operating. In Figs. 11(c) and 11(d), we have represented the corresponding time evolution of the 2n, $\langle r_{2n} \rangle$, and 3n, $\langle r_{3n} \rangle$, bond lengths for which a similar behavior is observed with
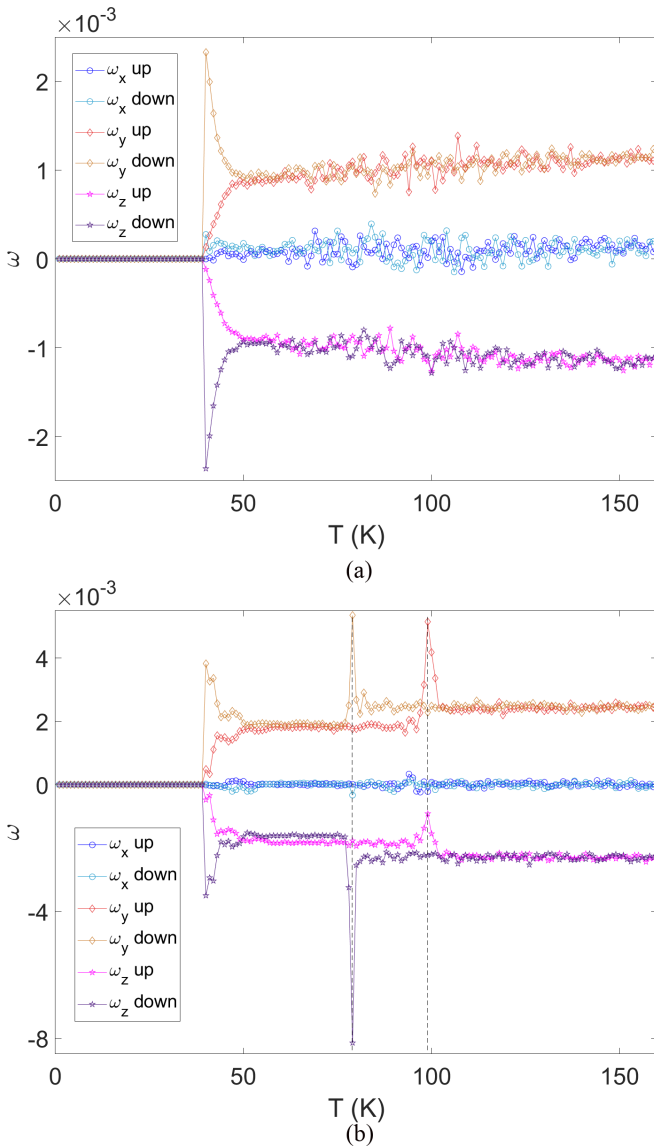
FIG. 10. Thermal dependence of the three components ω_x, ω_y, and ω_z of the rotation vector $\vec{\omega}$ during the heating-cooling cycle for two different values of elastic constants (a) $A_{1n} = 50$ for gradual transition and (b) $A_{1n} = 3000$ for hysteretic transition, where the presence of a hysteresis in ω_y and ω_z components is detected. The two vertical dashed lines indicate $T = 79$ and 99 K.

the two already defined regimes. In particular, the correlation between the HS fraction, n_{HS}, and the three nearest-neighbor bond lengths is more marked with $\langle r_{1n} \rangle$ for strong elastic constant, A_{1n}, values, where a two-step relaxation behavior is visible during the second regime. Moreover, one can clearly see that for smaller A_{1n} values (e.g., $A_{1n} = 50$, 100, and 250), the $2n$ and $3n$ lattice bondlengths, whose elastic constants ($A_{2n} = A_{3n} = 0.3A_{1n}$) are weaker than that of $1n$ sites, relax faster, following the already discussed deterministic regime. Besides, in Fig. 12, we draw the variation of the lifetime of the metastable state τ at $n_{HS} = 1/2$ as a function of the value of the elastic constant: a power law can be found. We plot a nonlinear regression using a logarithmic scale on the x and y axes, with a power law $\tau \sim (A_{1n})^\alpha$, with $\alpha \approx 4.41$.

Configurations of the lattice, Figs. 13, 14 and Fig. S10 of Ref. [60] during the relaxation process reveal interesting spatiotemporal aspects of the spin transition: multi-droplet behavior for weak values of elastic constant values A_{1n}, and cluster behavior for larger ones, in good agreement with the previous observation made on the thermal transition.

For weak values of A_{1n}, the weakness of cooperative interactions spreads the domain formation, and therefore the nucleation of the LS state takes place everywhere in the lattice with a ramified structure, as can be seen in spatiotemporal configurations of the lattice in Fig. S10 of Ref. [60].

For large values of A_{1n}, we see that four macroscopic LS domains located at the corners of the simulation starting from opposite tips of the lattice grow "independently" as far as they are far from each other, and advance towards the inner part of the sample, as represented in the spatiotemporal configurations of Fig. 13. It is consistent that nucleation of LS phase take place around the four corners of the lattice in a squared geometry, and spreads over the whole system, from energetic arguments. The spins in the corner (with only three nearest-neighbor $1n$) and on the edge (with only four nearest neighbors $1n$) are energetically preferable for the nucleation, which then explains the observations as well as those of the thermal hysteresis.

As an illustration, we present specific views of spatiotemporal configurations for $A_{1n} = 8000$ in Fig. 14 with only the LS spins visible during the transition to emphasize the nucleation and propagation processes: the $1n$ elastic constant becomes strong from this value, and to achieve the spin transition during the relaxation, we need to let almost 4000 MCS at $T = 10$ K in lieu of approximately 300 MCS at $T = 1$ K for $A_{1n} = 7000$. From this intensity of nearest-neighbor elastic constant, the nucleation and propagation process changes and a single cluster appears in a corner of the simulation cell, that propagates along the propagation direction, through a unique interface HS/LS, to reach the other side of the cell. The same pattern of nucleation at the very beginning of the MCS occurs, with the spins in the corner and on the edge are energetically preferable.

We display in Fig. 15(a) the spatial distribution of the local pressure field of the lattice for $A_{1n} = 8000$. To lighten the manuscript, we only show a sectional view in the plane (xOz) at $N_y/2$. The local pressure, P_i at site i, is calculated by the following expression (which is merely the gradient of the local elastic energy of the lattice at each site i): $P_i = -A_{1n} \sum_j (r_{ij} - R_0(S_i, S_j)) - B_{2n} \sum_k (r_{ik} - R'_0(S_i, S_k)) - C_{3n} \sum_p (r_{ip} - R''_0(S_i, S_p))$. This physical quantity is interesting because it provides additional information than the spatial distribution of the divergence of the displacement field. Actually the local pressure may be positive or negative according to the stress applied on the site: a compressive strain is equivalent to a positive pressure exerted on the site, while a tensile strain results in a negative pressure. Figure 15(a) provides detailed information concerning two important points: (i) the first one concerns the orientation of the front interface which changes from a tilted shape in the beginning of the transformation to a straight one around $t = 4151$ MCS as a result of the minimization of the total elastic energy by minimizing the interface length. Second (ii), we can see that the elastic strain deploys at long distance
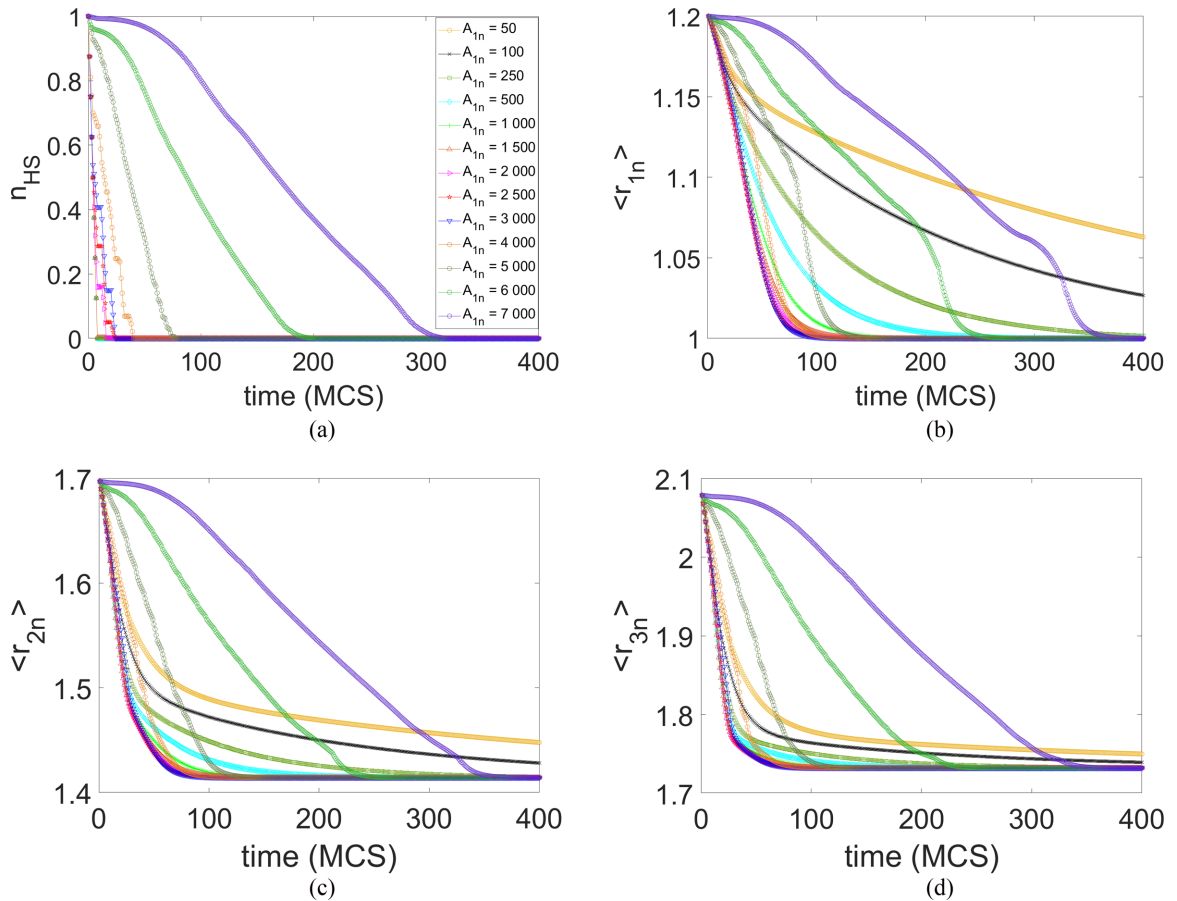
FIG. 11. Time dependence of the HS fraction (a) and average $1n$ (b), $2n$ (c), and $3n$ (d) lattice parameters along the relaxation from HS to LS of a lattice initially prepared in the HS state at low temperature ($T = 1$ K), for various elastic constant, A_{1n}, values. Remark the significant increase of the lifetime of the metastable state with respect to A_{1n}.

from both sides of the electronic HS/LS interface, where we see that the LS (respectively, HS) phase is experiencing a negative (respectively, positive) pressure. Overall, these re-
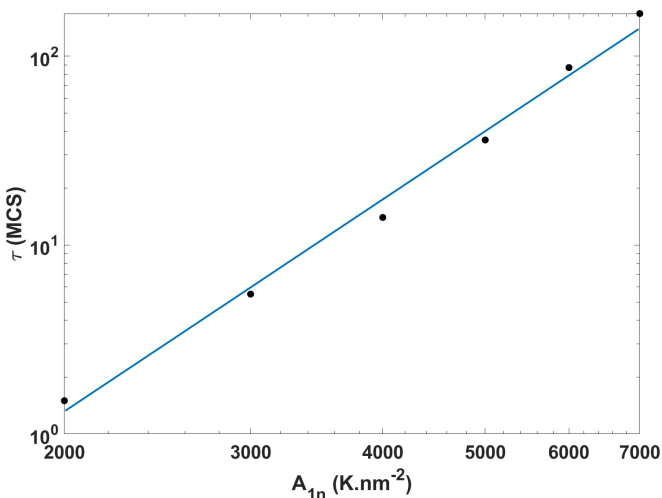
FIG. 12. Variation, in a log-log scale, of the lifetime of the metastable state τ, evaluated at $n_{HS} = 1/2$ in Fig. 11 as a function of A_{1n}, which fits with the linear regression (blue curve) with a slope $\alpha \simeq 4.4$, suggesting the power law $\tau \sim (A_{1n})^{4.4}$.

sults confirm the long-range nature of the elastic interactions as a driving force of the front propagation along the HS to LS relaxation. In Fig. 15(b), we show the distribution of the pressure in the plane (yOx) at $N_z/2$ for 4151 MCS: the same kind of behavior is observed, even if the interface seems to be more jagged in the y direction. Figure S11 of Ref. [60] highlight this sawlike pattern through planes (yOz) at various x direction values, from both sides of the interface, for 4151 MCS. We observe this peculiar blueprint for the distribution of the pressure around the interface. For views in the LS phase (between 44 and 39.5 nm) the tensile strain is obvious and occupies almost all the plane, while for the HS phase (between 39 and 33 nm), the compressive strain is visible, but with a concentric-serrated shape. It is important to notice that the latter is an artefact due to the meshing of the representation of the local pressure in the simulations. Actually, the propagation of the pressure wave is isotropic along the x propagation direction as displayed in Fig. S12 and the associated movie S5 inside [60], where we observe concave-shape in LS phase and convex one in the HS phase.

We study the energetic properties of this transformation through the dependence of the density of elastic energy, $\langle E_{\text{elastic}} \rangle$, of the lattice with respect to the growing LS fraction, $n_{LS} = (1 - n_{HS})$ [see Fig. 16(a)] during the relaxation process. Four distinct regimes are clearly identified. (i) First, a stationary regime, called here a stochastic regime, takes
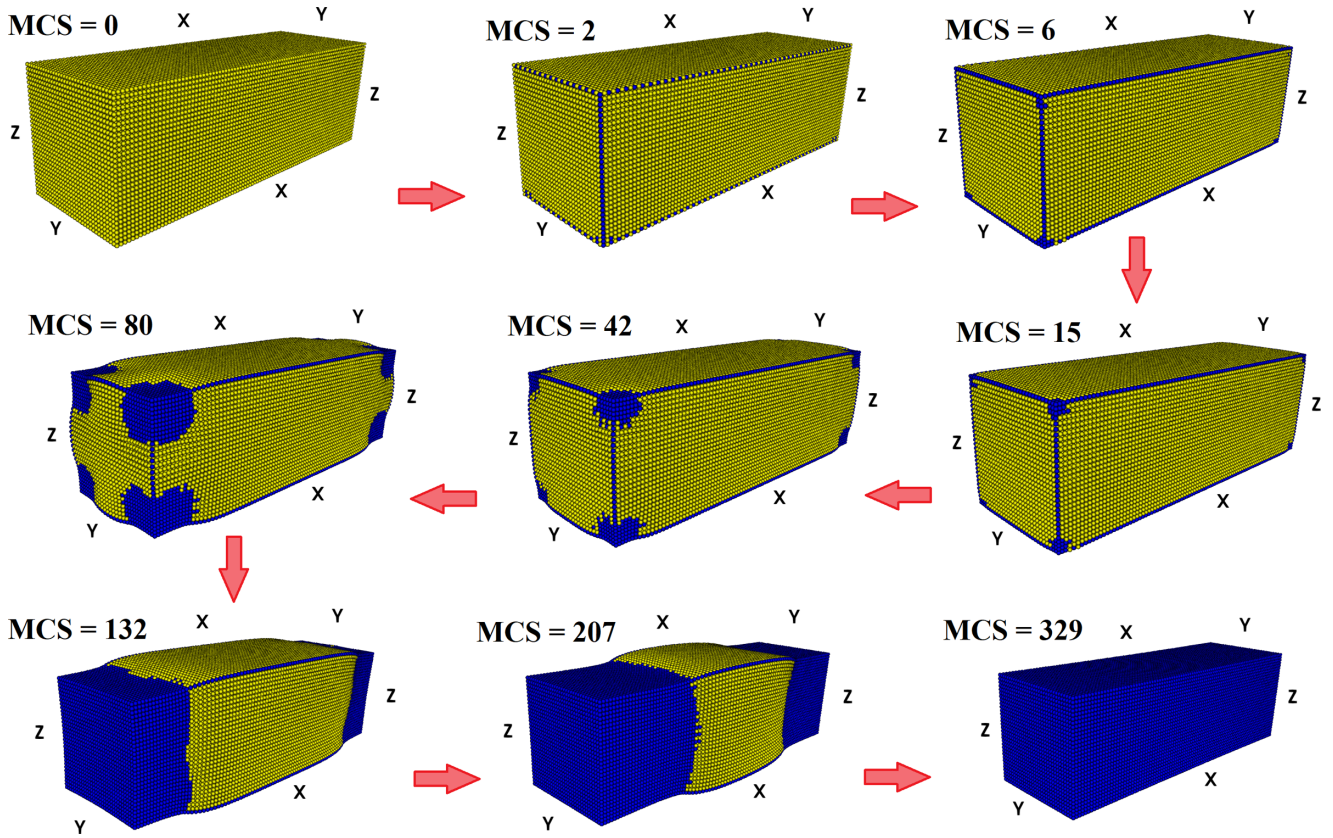
FIG. 13. Snapshots showing the spatiotemporal configurations of the lattice during the relaxation process at $T = 1$ K from an initial HS phase for a large $1n$ elastic constant value $A_{1n} = 7000$. Yellow (blue) spheres represent HS (LS) sites.

place around $n_{LS} = 0$, characterized by an important density of points in this location [see Fig. 16(a)], that lasts for a long time, ~ 3300 MCS, as shown in the corresponding Fig. 16(b). It is followed by a second regime (ii) where $\langle E_{elastic} \rangle$ rapidly increases in the interval of n_{LS} values ranging between 0 and 0.2 corresponding to the nucleation of LS phase from the lattice corner (see Fig. 14). This increase of the elastic energy is caused by the increase of the surface of the HS/LS interface, $S_{interf} = \pi R^2/8$ (R is the interface radius), along the growing LS domain size which has the shape of an eighth-sphere. When the radius of the sphere becomes equal to the lattice height or width $R = L_z$, the interface's surface goes through a maximum and so the elastic energy. At this point, the LS fraction can be roughly estimated as equal to the relative LS volume over the total lattice volume, i.e., $n_{LS} = \frac{\frac{1}{8} \frac{4}{3} \pi L_z^3}{L_z^2 L_x} \simeq 0.25$ which is in fair agreement with the value $n_{LS} \simeq 0.2$ derived form Fig. 16(a). In the third regime (iii), $\langle E_{elastic} \rangle$ goes through a minimum at $n_{LS} = 0.3$ corresponding to the change of the interface shape which adapts to the new boundary conditions imposed by the lattice borders. When the interface shape becomes stationary [i.e., straight and parallel to the (yOz) planes], it propagates keeping an invariant shape, which results in a flat and stationary elastic energy. The fourth regime (iv) corresponds to the so-called deterministic regime, during which the total energy decreases and the gain in the electronic energy largely compensates the elastic energy barrier [see Fig. 16(b) after the maximum]. Finally a rapid decrease of $\langle E_{elastic} \rangle$ occurs for $n_{LS} > 0.8$, corresponding to the

interface disappearance on the other side of the propagation axis.

Let us now briefly comment about the time-dependence of the density of total energy (DTE), given by DTE = $\Delta_{eff}(2n_{HS} - 1) + \langle E_{elastic} \rangle$. This quantity, displayed in Fig. 16(b), exhibits all the previous regimes discussed above. In particular, between 0 and 3500 MCS the system is in the stochastic regime and the DTE is almost constant to $DTE = +\Delta$ because the system occupies the HS state ($n_{HS} \sim 1$ and $\langle E_{elastic} \rangle \sim 0$). When the first LS nucleus appears, the DTE increases due to the appearance of elastic energy excess, which competes with the electronic energy, giving rise to a macroscopic energy barrier which peaks around 3700 MCS, a point which corresponds to the maximum surface of the HS/LS front interface. Beyond this point, the DTE quickly decreases, announcing the setting up of the deterministic/flow regime. Lastly, the DTE reaches a negative value almost constant to DTE $\simeq -\Delta$, when all spins are flipped to the LS state ($n_{HS} = 0$ and $\langle E_{elastic} \rangle \sim 0$). Another figure is presented in Fig. S13 of Ref. [60], showing the spatial distribution of the local elastic energy for the spatiotemporal configurations of the lattice given in Fig. 14, which confirm that the elastic energy is mainly stored around the HS/LS interface.

When one looks at the propagation front of Fig. 14 for $A_{1n} = 8000$, we would like to consider the spread of the elastic interface profiles. To do this, we calculate the Euclidean distance between two successive spins $\langle d \rangle$ along the propagation direction (Ox), by averages in (Oy) and (Oz)
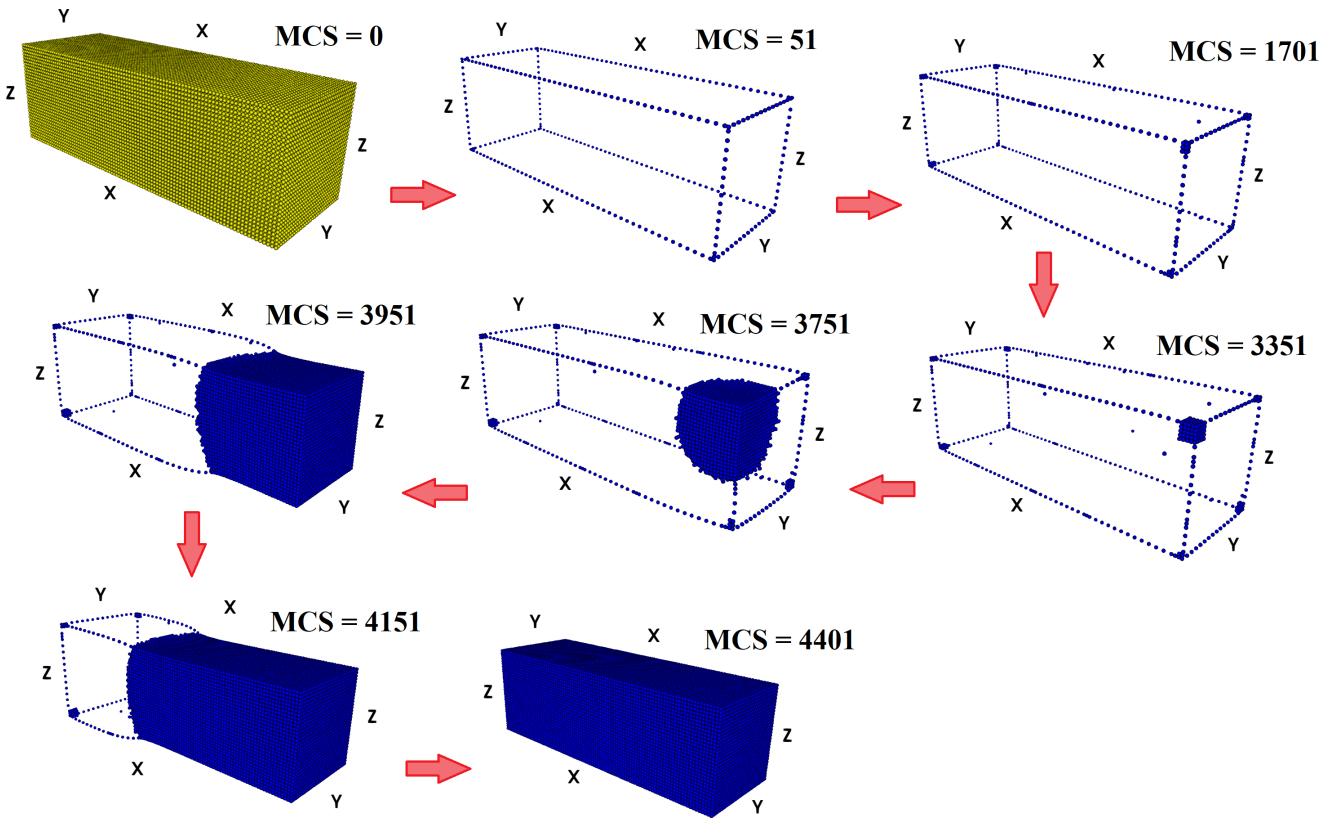
FIG. 14. Specific views of the snapshots showing the spatiotemporal configurations of the lattice during the relaxation process at $T = 10$ K from an initial HS phase for a large value $A_{1n} = 8000$, with only the LS spins visible during the transition. Yellow (blue) spheres represent HS (LS) sites.

directions: we draw different MCS values correlated to the established propagation front in the simulation cell, as can be seen in Fig. 17(a). Since in this case the propagation takes place from one corner with a unique interface HS/LS, we have to deal with one front coming from one side of the propagation axis, reaching the other side of the simulation cell. As we can see, the speed of propagation is constant, and a "cruising speed" is reached. The elastic interface is spatially wide, and cover a width of approximatively 20 nm. When approaching the interface, the LS region undergoes to compressive stress, while moving away the interface, the HS region goes through an expandable stress. To highlight this behavior, we have shown in Fig. 18 the spatial distribution of the local elastic energy field during the relaxation process in the plane (xOz) at $N_y/2$: one can simply visualize the broad width of the elastic interface confirming the assessment. This result is in agreement with experimental optical microscopy data of SCO single crystal [61]. Furthermore, this tends to imply that the shape of the HS/LS interface can adjust itself to the geometry of the system in order to reduce the total energy of the lattice. We compare these results with the spread of the electronic interface profiles for the same parameters, as shown in Fig. 17(b). Due to the propagation process, the same kind of behavior is observed with one front coming from one side of the propagation axis to the other. The electronic interface is spatially sharper and covers a width of approximately 8 nm, while the elastic interface is significantly broader (several tens

on nanometers) extending from both sides of the electronic interface.

IV. CONCLUSIONS

In this paper, we studied the thermal properties of the electroelastic 3D lattice, the macroscopic nucleation, growth, and propagation (NGP) of the front transformation during the spin transition in a 3D parallelepipedic shaped system.

We examined the shape of the thermal hysteresis of the HS fraction through the variation of the magnitude of the nearest-neighbor (1n) elastic constant, and we realized that above a critical threshold value of the 1n elastic constant, hysteresis arose out from elastic interactions. We analysed the dependence of the width of this thermal hysteresis window according to the 1n elastic constant value, and a power law emerged with an exponent approximately equal to 2. We performed an analysis on the dependence of the thermal HS fraction along the three directions (1,0,0), (0,1,0), and (0,0,1) of the lattice, and we pointed out a cascade effect along the extended direction of the simulation cell. A good correlation between the elastic variations of the lattice and the electronic variations of the spins during the hysteresis loop in thermal process has been displayed.

We investigated the NGP mechanisms along the thermal transition and similar tendencies as those observed in 2D lattices are found: above a critical value of the 1n elastic
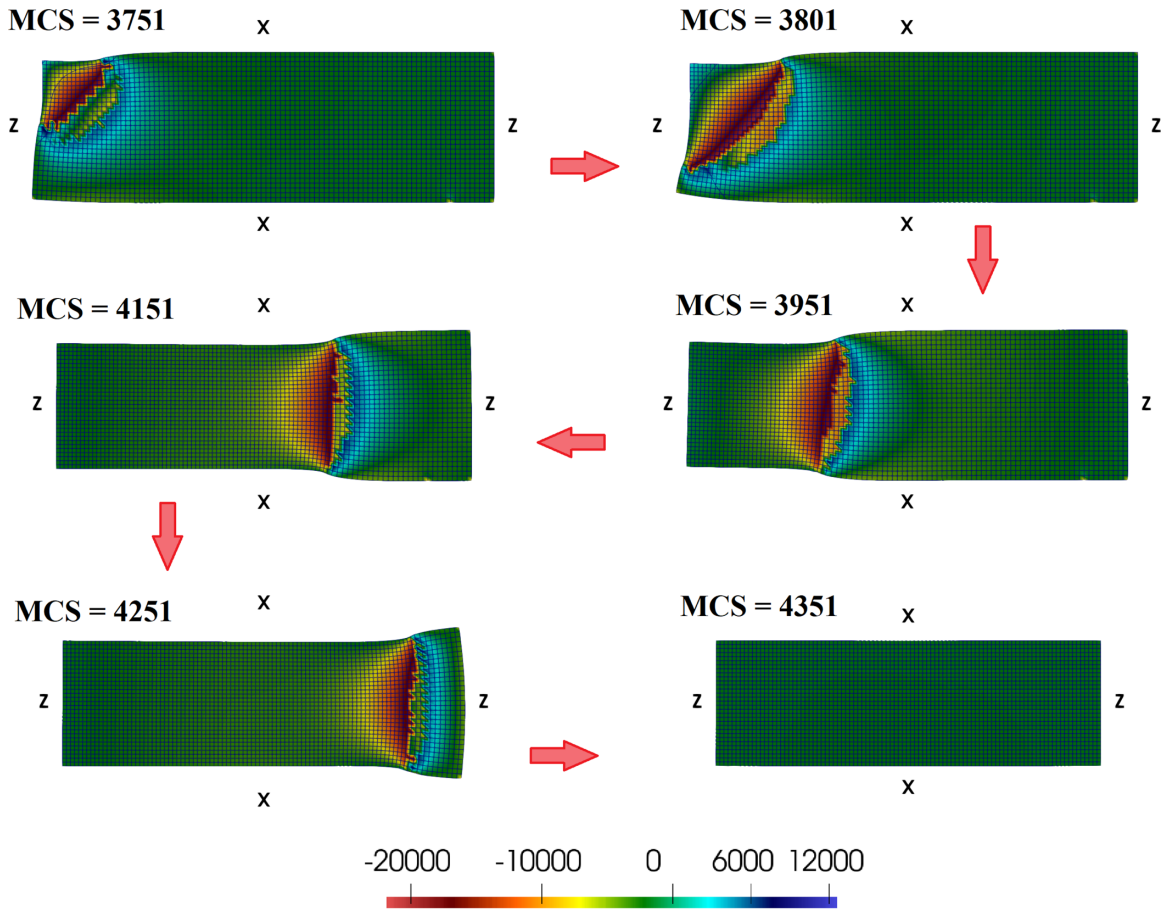
(a) View in the plane (xOz) at $\frac{N_y}{2}$ at various time (MCS).
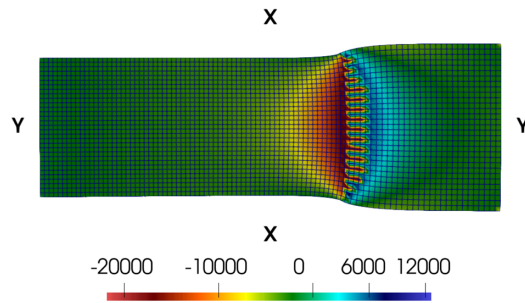
(b) View in the plane (yOx) at $\frac{N_z}{2}$ for 4 151 MCS.

FIG. 15. Sectional view in different planes showing the spatial distribution of the local pressure field of the lattice during the relaxation process at $T = 10$ K from an initial HS phase for a large value $A_{1n} = 8000$.

constant, the spin transition changed from random switching of the spin states to collective macroscopic domains starting from the corners of the simulation cell and propagating toward the inner part. We calculated the divergence of the displacement field, representing the relative volume expansion/contraction of the simulation cell, and a good agreement has been found between the spatiotemporal configurations of the spins and the divergence field during all the thermal transition. The interface shape was identified as being straight and perpendicular to the border of the cell thanks to that field.

We also computed the curl of the displacement field, accounting for the deviatoric strain in the lattice: during the heating branch a good correlation has been found with the spatiotemporal configurations, however there was a delay of some degrees for the appearance of the distorsion during the cooling branch compared to the propagation of the interface in spatiotemporal configurations (the distortion appeared before the interface in configurations). This phenomenon suggested a memory effect during the cooling branch relative to the heating branch happening in the first place.
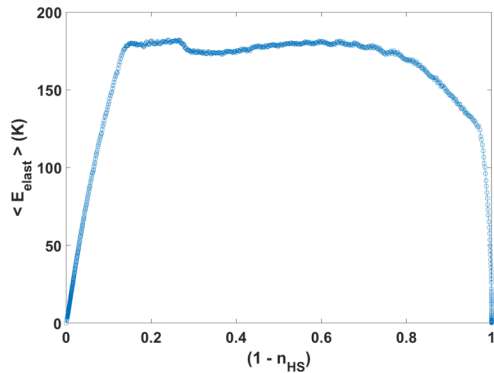
(a) LS fraction dependence of the elastic energy density showing a non-monotonous behavior along the relaxation process. See text for more explanations.
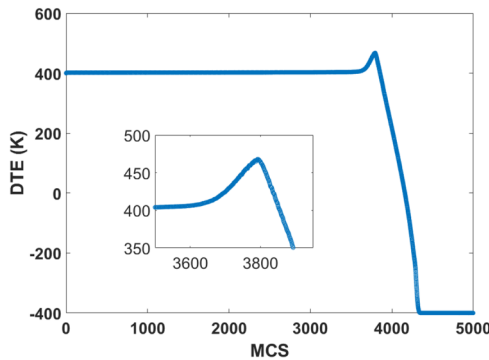
(b) Time-dependence of the DTE. Insert: zoom around the energy barrier of the DTE curve.

FIG. 16. Total elastic energy of the lattice in (a), and density of total energy (DTE) of the lattice in (b), during the relaxation process at $T = 10$ K from an initial HS phase for a large value $A_{1n} = 8000$. These results correspond to the spatiotemporal configurations of the lattice in Fig. 14; (a) LS fraction dependence of the elastic energy density showing a nonmonotonous behavior along the relaxation process. See text for more explanations. (b) Time dependence of the DTE. (Insert) Zoom around the energy barrier of the DTE curve.

We also investigated the NGP mechanisms over the relaxation process at low-temperature of the metastable HS state: the time dependence of the relaxation curves of the HS fraction confirmed the shift from weak cooperative to strong cooperative behavior when the $1n$ elastic constant increase. Moreover, for strong interactions the spatiotemporal configurations indicated that nucleation of LS phase take place around the corners of the lattice (on the edge and in the corner), spreading over the whole system toward the center of the simulation cell.

All of these results provided an overview of the 3D behavior of spin transition materials modeled by a electroelastic 3D lattice.

Among the possible developments of the present work, we quote: (i) the interesting extension to anisotropic elastic lattices by considering different A_{1n} values in three directions of space, which would be more consistent with the experimental reality of the materials studied in laboratory and (ii) the study of the lattice's shape effects by changing the simulation cell, or by considering different symmetry of the elementary cell is also an important objective of these 3D simulations. We could investigate under isotropic, or uniaxial, pressure to determine the effects on thermal transition and propagation dynamics of the HS/LS interface.
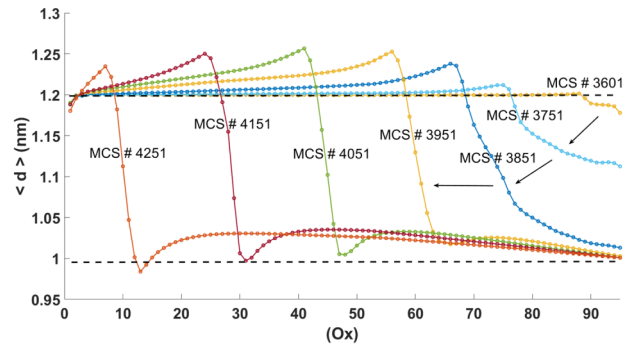
(a) Elastic interface profiles corresponding to the Euclidean distance between two successive spins. The dashed lines represent the equilibrium $1n$ distances $R_0^{HH} = 1.20$ nm and $R_0^{LL} = 1.00$ nm.
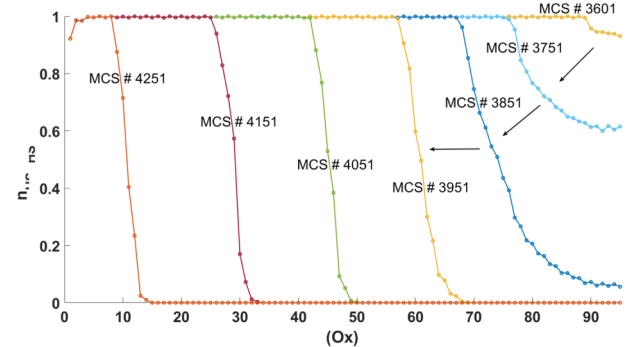
(b) Electronic interface profiles.

FIG. 17. Elastic and electronic interface profiles along the propagation direction (Ox) by averages in (Oy) and (Oz) directions. Some different MCS values correlated to the established propagation front of Fig. 14 have been shown. The arrows represent the propagation direction, as visual indicators; (a) Elastic interface profiles corresponding to the Euclidean distance between two successive spins. The dashed lines represent the equilibrium $1n$ distances $R_0^{HH} = 1.20$ nm and $R_0^{LL} = 1.00$ nm. (b) Electronic interface profiles.
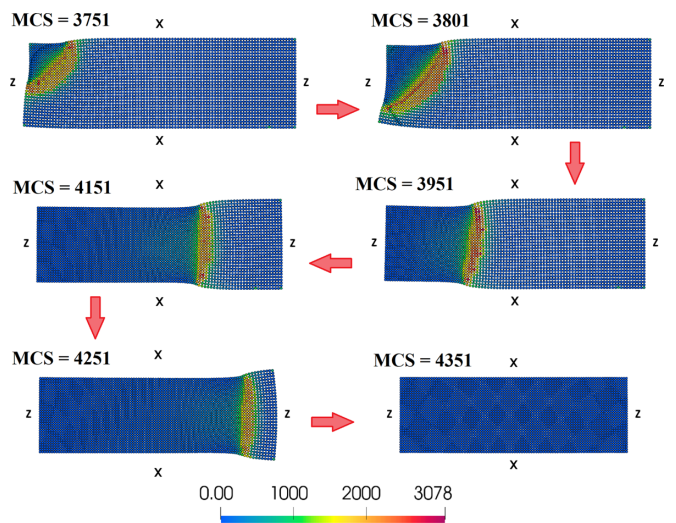
FIG. 18. Sectional view in the plane (xOz) at $N_y/2$ showing the spatial distribution of the local elastic energy field during the relaxation process at $T = 10$ K from an initial HS phase for a large value $A_{1n} = 8000$.

[1] E. König and B. Kanellakopulos, Mössbauer effect and magnetism down to 1.2 K in the triplet ground state of an iron(II)—phenanthroline complex, Chem. Phys. Lett. **12**, 485 (1972).

[2] O. Kahn and J.-P. Launay, Molecular bistability: An overview, J. P. Chemtronics **3**, 140 (1988).

[3] P. Gütlich, A. Hauser, and H. Spiering, de Thermal and Optical Switching of Iron(II) Complexes, Angew. Chem., Int. Ed. Engl. **33**, 2024 (1994).

[4] P. Gütlich and H. A. Goodwin, Spin Crossover – An Overall Perspective, in *Spin Crossover in Transition Metal Compounds I*, Topics in Current Chemistry, 233, edited by P. Gütlich and H. A. Goodwin (Springer, Berlin, Heidelberg, 2004).

[5] A. Bousseksou, G. Molnár, L. Salmon, and W. Nicolazzi, Molecular spin crossover phenomenon: recent achievements and prospects, Chem. Soc. Rev. **40**, 3313 (2011).

[6] O. Fouche, J. Degert, G. Jonusauskas, N. Daro, J.-F. Létard, and F. Eric, Mechanism for optical switching of the spin crossover [Fe(NH$_2$-trz)$_3$](Br)$_2$3H$_2$O compound at room temperature, Phys. Chem. Chem. Phys. **12**, 3044 (2010).

[7] A. Hauser, Spin-crossover materials. Properties and applications. Edited by Malcolm A. Halcrow, Angew. Chem. Int. Ed. **52**, 10419 (2013).

[8] C. M. Jureschi, J. Linares, A. Rotaru, M. H. Ritti, M. Parlier, M. M. Dîrtu, M. Wolff, and Y. Garcia, Pressure sensor via optical detection based on a 1D spin transition coordination polymer, Sensors **15**, 2388 (2015).

[9] H. Oyanagi, T. Tayagaki, and K. Tanaka, Synchrotron radiation study of photo-induced spin-crossover transitions: Microscopic origin of nonlinear phase transition, J. Lumin. Dynamical Processes in Excited States of Solids, **119**, 361 (2006).

[10] K. Boukheddaden, H. Fourati, Y. Singh, and G. Chastanet, Evidence of photo-thermal effects on the first-order thermo-induced spin transition of [{Fe(NCSe)(py)$_2$}$_2$(m-bpypz)] spin-crossover material, Magnetochemistry **5**, 21 (2019).

[11] P. Gütlich and H. A. Goodwin, *Spin Crossover in Transition Metal Compounds I–III*, Topics in Current Chemistry Vol. 233–235 (Springer, Berlin, Heidelberg, 2004).

[12] A. H. Ewald, R. L. Martin, I. G. Ross, A. H. White, and R. S. Nyholm, Anomalous behaviour at the 6A1-2T2 crossover in iron (III) complexes, Proc. R. Soc. London A **280**, 235 (1964).

[13] A. Desaix, O. Roubeau, J. Jeftic, J. G. Haasnoot, K. Boukheddaden, E. Codjovi, J. Linarès, M. Noguès, and F. Varret, Light-induced bistability in spin transition solids leading to thermal and optical hysteresis, Eur. Phys. J. B **6**, 183 (1998).

[14] P. Gütlich, A. Gaspar, V. Ksenofontov, and Y. Garcia, Pressure effect studies in molecular magnetism, J. Phys.: Condens. Matter **16**, S1087 (2004).

[15] S. Chorazy, T. Charytanowicz, D. Pinkowicz, J. Wang, K. Nakabayashi, S. Klimke, F. Renz, S.-I. Ohkoshi, and B. Sieklucka, Octacyanidorhenate(V) ion as an efficient linker for hysteretic two-step iron(II) spin crossover switchable by temperature, light, and pressure, Angew. Chem., Int. Ed. **59**, 15741 (2020).

[16] Y. Li, A. Benchohra, B. Xu, B. Baptiste, K. Béneut, P. Parisiades, L. Delbes, A. Soyer, K. Boukheddaden, and R. Lescouëzec, Pressure-induced conversion of a paramagnetic FeCo complex into a molecular magnetic switch with tuneable hysteresis, Angew. Chem. **132**, 17425 (2020).

[17] A. Bousseksou, F. Varret, M. Goiran, K. Boukheddaden, and J. P. Tuchagues, The Spin Crossover Phenomenon Under High Magnetic Field, in *Spin Crossover in Transition Metal Compounds III*, Topics in Current Chemistry, 235 (Springer, Berlin, Heidelberg, 2004).

[18] S. Decurtins, P. Gütlich, C. P. Köhler, H. Spiering, and A. Hauser, Light-induced excited spin state trapping in a transition-metal complex: The hexa-1-propyltetrazole-iron (II) tetrafluoroborate spin-crossover system, Chem. Phys. Lett. **105**, 1 (1984).

[19] P. Gütlich, Y. Garcia, and T. Woike, Photoswitchable coordination compounds, Coord. Chem. Rev. **219–221**, 839 (2001).

[20] M. Sy, D. Garrot, A. Slimani, M. Páez-Espejo, F. Varret, and K. Boukheddaden, Reversible control by light of the high-spin low-spin elastic interface inside the bistable region of a robust spin-transition single crystal, Angew. Chem. **128**, 1787 (2016).

[21] H. J. Shepherd, P. Rosa, I. A. Fallis, P. Guionneau, J. A. K. Howard, and A. E. Goeta, Structural origin of the gradual spin transition in a mononuclear iron(II) complex, J. Phys. Chem. Solids **73**, 193 (2012).

[22] K. Takahashi, H. Mori, H. Kobayashi, and O. Sato, Mechanism of reversible spin transition with a thermal hysteresis loop in [Fe^{III}(qsal)$_2$][Ni(dmise)$_2$]2CH$_3$CN: Selenium analogue of the precursor of an Fe(III) spin-crossover molecular conducting system, Polyhedron **28**, 1776 (2009).

[23] H. Spiering and N. Willenbacher, Elastic interaction of high-spin and low-spin complex molecules in spin-crossover compounds. II, J. Phys.: Condens. Matter **1**, 10089 (1989).

[24] C. Enachescu, J. Linarès, and F. Varret, Comparison of static and light-induced thermal hystereses of a spin-crossover solid, in a mean-field approach, J. Phys.: Condens. Matter **13**, 2481 (2001).

[25] H. Bolvin and O. Kahn, Ising model for low-spin high-spin transitions in molecular compounds; within and beyond the mean-field approximation, Chem. Phys. **192**, 295 (1995).

[26] K. Boukheddaden, I. Shteto, B. Hôo, and F. Varret, Dynamical model for spin-crossover solids. I. Relaxation effects in the mean-field approach, Phys. Rev. B **62**, 14796 (2000).

[27] F. Varret, S. A. Salunke, K. Boukheddaden, A. Bousseksou, É. Codjovi, C. Enachescu, and J. Linares, The Ising-like model applied to switchable inorganic solids : discussion of the static properties, Comptes Rendus Chimie **6**, 385 (2003).

[28] M. Nishino, K. Boukheddaden, Y. Konishi, and S. Miyashita, Simple Two-Dimensional Model for the Elastic Origin of

Cooperativity among Spin States of Spin-Crossover Complexes, Phys. Rev. Lett. **98**, 247203 (2007).

[29] C. Enachescu, M. Nishino, S. Miyashita, A. Hauser, A. Stancu, and L. Stoleriu, Cluster evolution in spin crossover systems observed in the frame of a mechano-elastic model, Europhys. Lett. **91**, 27003 (2010).

[30] C. Enachescu, M. Nishino, S. Miyashita, K. Boukheddaden, F. Varret, and P. A. Rikvold, Shape effects on the cluster spreading process of spin-crossover compounds analyzed within an elastic model with Eden and Kawasaki dynamics, Phys. Rev. B **91**, 104102 (2015).

[31] W. Nicolazzi, S. Pillet, and C. Lecomte, Two-variable anharmonic model for spin-crossover solids: A like-spin domains interpretation, Phys. Rev. B **78**, 174401 (2008).

[32] W. Nicolazzi, J. Pavlik, S. Bedoui, G. Molnár, and A. Bousseksou, Elastic Ising-like model for the nucleation and domain formation in spin crossover molecular solids, Eur. Phys. J.: Spec. Top. **222**, 1137 (2013).

[33] A. Slimani, K. Boukheddaden, F. Varret, H. Oubouchou, M. Nishino, and S. Miyashita, Microscopic spin-distortion model for switchable molecular solids: Spatiotemporal study of the deformation field and local stress at the thermal spin transition, Phys. Rev. B **87**, 014111 (2013).

[34] M. Ndiaye and K. Boukheddaden, Electro-elastic modelling of the two-step high-spin to low-spin relaxation with transient self-organized spin states in 2D spin crossover solids, J. Phys. Soc. Jpn. **89**, 014004 (2020).

[35] C. Chong, H. Mishra, K. Boukheddaden, S. Denise, G. Bouchez, E. Collet, J.-C. Ameline, A. D. Naik, Y. Garcia, and F. Varret, Electronic and structural aspects of spin transitions observed by optical microscopy. The case of [Fe(ptz)$_6$](BF$_4$)$_2$, J. Phys. Chem. B **114**, 1975 (2010).

[36] A. Slimani, F. Varret, K. Boukheddaden, D. Garrot, H. Oubouchou, and S. Kaizaki, Velocity of the High-Spin Low-Spin Interface Inside the Thermal Hysteresis Loop of a Spin-Crossover Crystal, via Photothermal Control of the Interface Motion, Phys. Rev. Lett. **110**, 087208 (2013).

[37] Y. Konishi, H. Tokoro, M. Nishino, and S. Miyashita, Monte Carlo Simulation of Pressure-Induced Phase Transitions in Spin-Crossover Materials, Phys. Rev. Lett. **100**, 067206 (2008).

[38] C. Enachescu, L. Stoleriu, A. Stancu, and A. Hauser, Model for Elastic Relaxation Phenomena in Finite 2D Hexagonal Molecular Lattices, Phys. Rev. Lett. **102**, 257204 (2009).

[39] M. Nishino, C. Enachescu, S. Miyashita, P. A. Rikvold, K. Boukheddaden, and F. Varret, Macroscopic nucleation phenomena in continuum media with long-range interactions, Sci. Rep. **1**, 162 (2011).

[40] C. Enachescu and W. Nicolazzi, Elastic models, lattice dynamics and finite size effects in molecular spin crossover systems, Comptes Rendus Chimie **21**, 1179 (2018).

[41] M. Nishino, Y. Singh, K. Boukheddaden, and S. Miyashita, Tutorial on elastic interaction models for multistep spin-crossover transitions, J. Appl. Phys. **130**, 141102 (2021).

[42] K. Boukheddaden and A. Bailly-Reyre, Towards the elastic properties of 3D spin-crossover thin films: Evidence of buckling effects, Europhys. Lett. **103**, 26005 (2013).

[43] L. Stoleriu, M. Nishino, S. Miyashita, A. Stancu, A. Hauser, and C. Enachescu, Cluster evolution in molecular three-dimensional spin-crossover systems, Phys. Rev. B **96**, 064115 (2017).

[44] S. Rohlf, J. Grunwald, T. Jasper-Toennies, S. Johannsen, F. Diekmann, M. Studniarek, R. Berndt, F. Tuczek, K. Rossnagel, and M. Gruber, Influence of substrate electronic properties on the integrity and functionality of an adsorbed fe(ii) spin-crossover compound, J. Phys. Chem. C **123**, 17774 (2019).

[45] K. Affes, A. Slimani, Y. Singh, A. Maalej, and K. Boukheddaden, Magneto-elastic properties of a spin crossover membrane deposited on a deformable substrate, J. Phys.: Condens. Matter **32**, 255402 (2020).

[46] A.-I. Popa, L. Stoleriu, and C. Enachescu, Tutorial on the elastic theory of spin crossover materials, J. Appl. Phys. **129**, 131101 (2021).

[47] K. S. Kumar and M. Ruben, Sublimable spin-crossover complexes: From spin-state switching to molecular devices, Angew. Chem. Int. Ed. **60**, 7502 (2021).

[48] M. Kelai, V. Repain, A. Tauzin, W. Li, Y. Girard, J. Lagoute, S. Rousset, E. Otero, P. Sainctavit, M.-A. Arrio, M.-L. Boillot, T. Mallah, C. Enachescu, and A. Bellec, Thermal bistability of an ultrathin film of iron(II) spin-crossover molecules directly adsorbed on a metal surface, J. Phys. Chem. Lett. **12**, 6152 (2021).

[49] R. Sánchez-de-Armas, N. Montenegro-Pohlhammer, A. Develioglu, E. Burzuri, and C. J. Calzado, Spin-crossover complexes in nanoscale devices: main ingredients of the molecule substrate interactions, Nanoscale **13**, 18702 (2021).

[50] A. Slimani, K. Boukheddaden, and K. Yamashita, Effect of intermolecular interactions on the nucleation, growth, and propagation of like-spin domains in spin-crossover materials, Phys. Rev. B **92**, 014111 (2015).

[51] R. Traiche, H. Oubouchou, M. Zergoug, and K. Boukheddaden, Spatio-temporal aspects of the domain propagation in a spin-crossover lattice with defect, Phys. B: Condens. Matter **516**, 77 (2017).

[52] J. Jung, F. Bruchhäuser, R. Feile, H. Spiering, and P. Gütlich, The cooperative spin transition in [|Fe$_x$Zn$_{1-x}$(ptz)$_6$](BF$_4$)$_2$: I. Elastic properties—an oriented sample rotation study by Brillouin spectroscopy, Z. Phys. B **100**, 517 (1996).

[53] M. Paez-Espejo, M. Sy, and K. Boukheddaden, Elastic frustration causing two-step and multistep transitions in spin-crossover solids: Emergence of complex antiferroelastic structures, J. Am. Chem. Soc. **138**, 3202 (2016).

[54] R. H. Swendsen and J.-S. Wang, Nonuniversal critical dynamics in Monte Carlo simulations, Phys. Rev. Lett. **58**, 86 (1987).

[55] A. Bousseksou, C. Place, J. Linares, and F. Varret, Dynamic spin crossover in [Fe(2-BIK)$_3$](ClO$_4$)$_2$ and [Fe(Me$_2$2-BIK)$_3$](BF$_4$)$_2$ investigated by mossbauer spectroscopy, J. Magn. Magn. Mater. **104–107**, 225 (1992).

[56] P. Adler, A. Hauser, A. Vef, H. Spiering, and P. Gutlich, Dynamics of spin state conversion processes in the solid state, Hyperfine Interact. **47–48**, 343 (1989).

[57] P. Adler, H. Spiering, and P. Gutlich, Thermodynamics and kinetics of spin state conversion processes studied by pressure dependent mossbauer spectroscopy, J. Phys. Chem. Solids **50**, 587 (1989).

[58] T. H. Group, Hierarchical Data Format, version 5 (1997).

[59] L. Stoleriu, P. Chakraborty, A. Hauser, A. Stancu, and C. Enachescu, Thermal hysteresis in spin-crossover compounds studied within the mechanoelastic model and its potential application to nanoparticles, Phys. Rev. B **84**, 134102 (2011).

[60] See Supplemental Material at http://link.aps.org/supplemental/10.1103/PhysRevB.106.014422 for (i) movies of the evolution of the spatiotemporal configurations of the lattice during the thermal cycles for different values of the elastic constants, and spatial distribution of the elastic energy and pressure field; (ii) interplay between dynamics of the spin and lattice degrees of freedom along the thermal transition; (iii) the thermal dependence of the first-, second-, and third-nearest-neighbor distances along the thermal hysteresis; (iv) spatial distribution of the divergence and curl of divergence fields along the thermal transition; and (v) selected snapshots of spatiotemporal lattice configuration and pressure field along the low-temperature relaxation from high spin to low spin state.

[61] A. Slimani, F. Varret, K. Boukheddaden, C. Chong, H. Mishra, J. Haasnoot, and S. Pillet, Visualization and quantitative analysis of spatiotemporal behavior in a first-order thermal spin transition: A stress-driven multiscale process, Phys. Rev. B **84**, 094442 (2011).